

# Uncertainty Quantification of Ship Resistance via Multi-Index Stochastic Collocation and Radial Basis Function Surrogates: A Comparison

Chiara Piazzola\* and Lorenzo Tamellini†

*CNR-IMATI, National Research Council-Institute for Applied Mathematics and Information Technologies  
“E. Magenes”, Pavia, Italy*

Riccardo Pellegrini‡, Riccardo Broglia§, Andrea Serani¶, and Matteo Diez||  
*CNR-INM, National Research Council-Institute of Marine Engineering, Rome, Italy*

**This paper presents a comparison of two methods for the forward uncertainty quantification (UQ) of complex industrial problems. Specifically, the performance of Multi-Index Stochastic Collocation (MISC) and adaptive multi-fidelity Stochastic Radial Basis Functions (SRBF) surrogates is assessed for the UQ of a roll-on/roll-off passengers ferry advancing in calm water and subject to two operational uncertainties, namely the ship speed and draught. The estimation of expected value, standard deviation, and probability density function of the (model-scale) resistance is presented and discussed obtained by multi-grid Reynolds averaged Navier-Stokes (RANS) computations. Both MISC and SRBF use as multi-fidelity levels the evaluations on different grid levels, intrinsically employed by the RANS solver for multi-grid acceleration; four grid levels are used here, obtained as isotropic coarsening of the initial finest mesh. The results suggest that MISC could be preferred when only limited data sets are available. For larger data sets both MISC and SRBF represent a valid option, with a slight preference for SRBF, due to its robustness to noise.**

## I. Introduction

SHIP performance depends on design and operational/environmental parameters. The accurate prediction of significant design metrics (such as resistance and powering requirements; seakeeping, maneuverability, and dynamic stability; structural response and failure) requires prime-principles-based high-fidelity computational tools (e.g., computational fluid/structural dynamics, CFD/CSD), especially for innovative configurations and off-design conditions. These tools are generally computationally expensive, making the exploration of design and operational-uncertainty (such as in uncertainty quantification, UQ) spaces a technological challenge. The development and application of UQ methods for vehicle problems (including ships) were the subject of the NATO Science and Technology Organization, Applied Vehicle Technology group AVT-191 “Application of Sensitivity Analysis and Uncertainty Quantification to Military Vehicle Design,” where the UQ of a high-speed catamaran in irregular head waves was performed via both CFD computations [1, 2] and towing-tank experiments [3]. UQ methods for ship operational parameters are an essential element of reliability-based and robust design optimization for vessels sailing in real-world stochastic conditions [4]. The integration of UQ methods within stochastic design optimization procedures for vehicle problems was addressed in the AVT-252 group on “Stochastic Design Optimization for Naval and Aero Military Vehicles,” where the hull form of a naval destroyer was optimized for stochastic ocean conditions [5]. The group also addressed the application of several UQ methods (including multi-fidelity approaches) to an airfoil benchmark problem and the results were discussed in [6]. Finally, the application of multi-fidelity methodologies to the analysis and design of vehicles is addressed by the AVT-331 group on “Goal-Driven, Multi-Fidelity Approaches for Military Vehicle System-Level Design.” An overview on the AVT-331 activities on multi-fidelity approaches may be found in [7].

\*Postdoctoral Research Fellow, CNR-IMATI Pavia, Via Adolfo Ferrata 5/A, 27100

†Research Scientist, CNR-IMATI Pavia, Via Adolfo Ferrata 5/A, 27100

‡Postdoctoral Research Fellow, CNR-INM Rome, Via di Vallerano 139, 00128

§Research Scientist, CNR-INM Rome, Via di Vallerano 139, 00128

¶Research Scientist, CNR-INM Rome, Via di Vallerano 139, 00128

||Senior Research Scientist, CNR-INM Rome, Via di Vallerano 139, 00128, AIAA Member, Email: matteo.diez@cnr.it

There is by now a large consensus also in the UQ community on the fact that large-scale, industrially relevant UQ analyses can only be performed by leveraging on multi-fidelity methodologies, i.e., methodologies that explore the bulk of the variability of the quantities of interest of the simulation over coarse meshes (or more generally, computationally inexpensive models with e.g. simplified physics), and resort to querying high-fidelity models (e.g., refined meshes or full-physics models) only sparingly, to correct the initial guess produced with the low-fidelity models. Several approaches to this general framework can be conceived, depending on the kind of fidelity models considered and on the strategy used to sample the parameter space (i.e., for what values of the uncertain parameters the different fidelity models should be queried/evaluated).

In this context, the family of multi-level/multi-index methods has received an increasing attention, due to its effectiveness and solid mathematical ground. The hierarchy of models considered by these methods is usually obtained by successive (dyadic) refinements of a computational mesh. The multi-level/multi-index distinction arises from the number of discretization parameters that are considered to generate the sequence of meshes: playing with a single mesh-element-size parameter  $h$  results in the “multi-level” version of the method, while considering multiple parameters (e.g., quadrilateral/hexahedral meshes with multiple size parameters  $h_1, h_2, h_3$  chosen independently and/or time stepping) results in the “multi-index” version of the method. Combining this mesh-generation strategy with a specific sampling strategy over the parameter space results in the different variations of the method, such as Multi-Level Monte-Carlo (the first one to be proposed, [8, 9]), Multi-Index Monte Carlo [10], Multi-Level/Multi-Index Quasi-Monte-Carlo [11], Multi-Level Stochastic Collocation [12], Multi-Index Stochastic Collocation [13, 14], Multi-Level Least-Squares polynomial approximation [15], etc. The multi-level/multi-index framework can also be extended to the more generic scenario of Monte-Carlo sampling of multiple fidelities (e.g. combining different physical models), see e.g. [16, 17]. See also e.g. [18–20] for applications of Multi-Level Monte-Carlo approaches in the context of aerodynamics.

Another widely studied class of multi-fidelity methods employs kernel-based surrogates such as hierarchical kriging [21], co-kriging [22], Gaussian process [23], and radial-basis functions [24]. Additive, multiplicative, or hybrid correction methods, also known as “bridge functions” or “scaling functions” [25], are used to build multi-fidelity surrogates. Further efficiency of multi-fidelity surrogates is gained using dynamic/adaptive sampling strategies, for which the multi-fidelity design of experiments for the surrogate training is not defined a priori but dynamically updated, exploiting the information that becomes available during the training process. Training points are dynamically added with the automatic selection of their location and the desired fidelity level, to the aim of reducing the computational cost required to properly represent the function. An example of adaptive multi-fidelity sampling based on the maximum prediction uncertainty is given in [24].

The objective of the present work is to assess and compare the use of two methods from these two methodological families for the forward UQ of complex industrial problems. Specifically, the performances of Multi-Index Stochastic Collocation (MISC, [13, 14]) and adaptive Multi-Fidelity Stochastic Radial Basis Functions (SRBF [23]) are compared on the UQ of a roll-on/roll-off passengers (RoPax) ferry sailing in calm water with two operational uncertainties, specifically ship speed and draught, the latter being directly linked to the payload. The estimation of expected value, standard deviation, and probability density function of the (model-scale) resistance, are presented and discussed. Ship performance are assessed by CFD computations based on a Reynolds averaged Navier-Stokes (RANS) equations solver:  $\chi$ navis [26–28], developed at CNR-INM. Both MISC and SRBF use as fidelity levels the intermediate grids employed by the URANS solver (which is a multi-grid solver): these grids – four in total – are obtained as isotropic refinement of an initial coarse grid. Therefore, both MISC and SRBF are used as multi-index methods with only one component controlling the spatial discretization.

## II. Forward Uncertainty Quantification Method

Let us consider a single-patch mesh of the computational domain with non-cubic hexahedral elements of the same size\* and let us also assume that the level of refinement of the mesh along each physical direction can be specified by prescribing some user-defined integer values  $\alpha_1, \alpha_2, \alpha_3$ ; to fix ideas, one can think e.g. that the size of each element of the mesh scales as  $2^{-\alpha_1} \times 2^{-\alpha_2} \times 2^{-\alpha_3}$ , but this is not necessary. The three values of  $\alpha_i$  are collected in a multi-index  $\alpha = [\alpha_1, \alpha_2, \alpha_3]$ ; prescribing the multi-index  $\alpha$  thus prescribes the computational mesh to be generated. If this flexibility is not allowed by the mesh-generator (or by the problem itself), it is possible to set  $\alpha_1 = \alpha_2 = \alpha_3 = \alpha$ , i.e., controlling the mesh-generation by a single integer value  $\alpha$ . The same philosophy applies also to multi-patch meshes, where in principle there could be up to three values  $\alpha_i$  for each patch. The quantity of interest of the CFD simulation computed over the mesh specified by  $\alpha$  is denoted by  $G_\alpha$ ; this could be either the full velocity field or a scalar quantity associated

---

\*this assumption can be relaxed, but it is kept for simplicity of exposition

to it.

Next, let us assume that the CFD simulation depends on the value of one or more random/uncertain parameters, say  $N$  parameters collected in the random vector  $\mathbf{y} = [y_1, y_2, \dots, y_N]$ . Denote by  $\Gamma$  the set of all possible values of  $\mathbf{y}$ , and by  $\rho(\mathbf{y})$  the probability density function (PDF) of the random vector  $\mathbf{y}$  over  $\Gamma$ . Thus, the primary goal of the forward UQ analysis is to compute an approximation of  $\mathbb{E}[G_\alpha]$ , i.e., of the expected value of  $G_\alpha$ . This quantity is typically computed by a sampling approach, i.e., the partial differential equation (PDE) at hand is solved (i.e. the CFD simulation is performed over the grid indexed by  $\alpha$ ) for several possible values of  $\mathbf{y}$ , and the results are averaged with some weights:

$$\mathbb{E}[G_\alpha] \approx \sum_{j=1}^J G_\alpha(\mathbf{y}_j) \omega_j. \quad (1)$$

The simplest averaging scheme is Monte Carlo, where the values  $\mathbf{y}_j$  are chosen at random over  $\Gamma$  (according to the PDF  $\rho$ ) and  $\omega_j = 1/J$ . Other quantities can be object of the forward UQ analysis, e.g. the standard deviation  $\text{std}[G_\alpha] = \mathbb{E}[G_\alpha^2] - \mathbb{E}[G_\alpha]^2$  or the PDF of  $G_\alpha$ . More details on the computation of the latter will be given in Sect. IV.

### A. Multi-Index Stochastic Collocation

Roughly speaking, MISC is based on using as points  $\mathbf{y}_j$  the union of several Cartesian grids over the domain  $\Gamma$ , that are obtained by tensorization of univariate quadrature rules (which should be chosen according to  $\rho(\mathbf{y})$  for computational efficiency). In this work  $y_1, y_2, \dots, y_N$  are uniform and independent random variables (see Section III) and the univariate Clenshaw–Curtis (CC) quadrature is employed. The collocation points for the  $K$ -points CC quadrature rule are

$$t_{j,K} = \cos\left(\frac{(j-1)\pi}{K-1}\right), \quad 1 \leq j \leq K,$$

and the corresponding quadrature weights can be efficiently computed by fast Fourier transform, see e.g. [29]. Similarly to what done with the multi-index  $\alpha$  for the physical domain, a multi-index  $\beta \in \mathbb{N}^N$  is introduced, that specifies how many points  $\mathbf{y}$  will be used to generate one of the above mentioned Cartesian grids. More specifically, after having introduced the auxiliary function

$$m(0) = 0, \quad m(1) = 1, \quad m(i) = 2^{i-1} + 1 \text{ for } i \geq 2, \quad (2)$$

$m(\beta_1)$  CC points are generated for  $y_1$ ,  $m(\beta_2)$  CC points are generated for  $y_2$  etc., and the grid obtained by taking the Cartesian product of the  $N$  sets of points thus generated is considered. Note that this choice of  $m$  guarantees that, given any two multi-indices  $\beta_1$  and  $\beta_2$ , the grid obtained using  $\beta_1$  is contained (*nested*) in the one obtained using  $\beta_2$  whenever all components of  $\beta_1$  are smaller or equal than the corresponding components in  $\beta_2$ . This is clearly useful in the context of adaptive schemes, like the version of MISC that we advocate in this work. The quadrature weight  $\omega_j$  of each point of the Cartesian grid is immediately obtained by taking the product of the corresponding univariate weights.

The approximation of  $\mathbb{E}[G_\alpha]$  computed over this grid with Eq. 1 is denoted as  $Q_{\alpha,\beta}$ . Clearly, it would be beneficial to have both multi-indices  $\alpha$  and  $\beta$  with large components, say  $\alpha = \alpha^\star$  and  $\beta = \beta^\star$ , i.e., to average the values of many PDE solutions over a refined computational mesh. However, this is typically unfeasible due to computational costs. One possible remedy is to exploit the fact that a single, highly refined approximation  $Q_{\alpha^\star,\beta^\star}$  can often<sup>†</sup> be approximated as a linear combination of many coarser  $Q_{\alpha,\beta}$ , where whenever the spatial discretization  $\alpha$  is refined, the quadrature level  $\beta$  is kept to a minimum and viceversa (of course, the combined cost of computing the set of coarse discretizations should be smaller than the cost of the highly refined one). This is in a nutshell the idea of MISC. In other words, MISC is a classical multi-level scheme, where most of the statistical variability of  $G$  is explored by solving many PDEs with coarse meshes (large  $\|\beta\|^\ddagger$  with small  $\|\alpha\|$ ) and then the result is corrected with a few PDE solutions with refined meshes (large  $\|\alpha\|$  with small  $\|\beta\|$ ). Clearly, as all multi-level approaches, MISC works well only if the levels are sufficiently separated, i.e. if the number of degrees of freedom (and the corresponding computational cost) grows significantly from one level to the next one: to fix ideas again, things will work if the number of elements in the mesh scales e.g. as  $2^{\alpha_1} \times 2^{\alpha_2} \times 2^{\alpha_3}$ , but not if e.g. increasing  $\alpha_1$  to  $\alpha_1 + 1$  adds only one element to the mesh.

In the following the details of MISC are briefly recalled, following closely the setup in [13]. Firstly, the so-called univariate and multivariate “detail operators” on the physical and stochastic domains have to be introduced. They are

<sup>†</sup> whenever  $G(\mathbf{y})$  is a smooth function with respect to  $\mathbf{y}$ , i.e., small changes in  $\mathbf{y}$  imply small changes in  $G(\mathbf{y})$

<sup>‡</sup>  $\|\cdot\|$  denotes the Euclidean norm

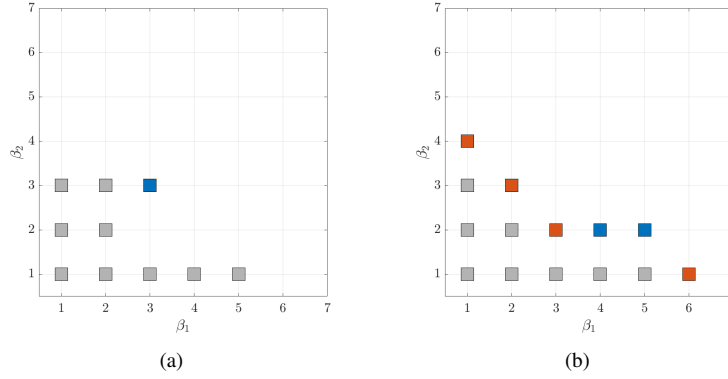


**Fig. 1** (a): the gray set is downward closed, whereas adding the blue multi-index to it would result in a set not downward closed; (b): a downward closed set (in gray) and its margin (indices marked in red and blue). If Algorithm 1 reaches the gray set, it will next explore all indices marked in red (their addition to the gray set keeps the downward closedness property) but not those marked in blue. The red set is also known as “reduced margin”.

defined as follows, with the understanding that  $Q_{\alpha,\beta} = 0$  when at least one component of  $\alpha$  or  $\beta$  is zero:

**Univariate physical detail:**  $\Delta_i^{\text{phys}}[Q_{\alpha,\beta}] = Q_{\alpha,\beta} - Q_{\alpha - \mathbf{e}_i, \beta}$  with  $1 \leq i \leq 3$ ;

**Univariate stochastic detail:**  $\Delta_i^{\text{stoc}}[Q_{\alpha,\beta}] = Q_{\alpha,\beta} - Q_{\alpha, \beta - \mathbf{e}_i}$  with  $1 \leq i \leq N$ ;

**Multivariate physical detail:**  $\Delta^{\text{phys}}[Q_{\alpha,\beta}] = \bigotimes_{i=1}^3 \Delta_i^{\text{phys}}[Q_{\alpha,\beta}];$

**Multivariate stochastic detail:**  $\Delta^{\text{stoc}}[Q_{\alpha,\beta}] = \bigotimes_{j=1}^N \Delta_j^{\text{stoc}}[Q_{\alpha,\beta}];$

**Mixed multivariate detail:**  $\Delta^{\text{mix}}[Q_{\alpha,\beta}] = \Delta^{\text{stoc}}[\Delta^{\text{phys}}[Q_{\alpha,\beta}]].$

Note that  $\mathbf{e}_i$  denotes the canonical multi-index, i.e.  $(\mathbf{e}_i)_k = 1$  if  $i = k$  and 0 otherwise. Observe that taking tensor products of univariate details amounts to composing their actions, e.g.,

$$\Delta^{\text{phys}}[Q_{\alpha,\beta}] = \bigotimes_{i=1}^3 \Delta_i^{\text{phys}}[Q_{\alpha,\beta}] = \Delta_1^{\text{phys}} \left[ \Delta_2^{\text{phys}} \left[ \Delta_3^{\text{phys}} [Q_{\alpha,\beta}] \right] \right],$$

and analogously for the stochastic multivariate detail operators,  $\Delta^{\text{stoc}}[Q_{\alpha,\beta}]$ . Crucially, this in turn implies that the multivariate operators can be evaluated by evaluating certain full-tensor approximations  $Q_{\alpha,\beta}$  and then taking linear combinations:

$$\Delta^{\text{phys}}[Q_{\alpha,\beta}] = \Delta_1^{\text{phys}} \left[ \Delta_2^{\text{phys}} \left[ \Delta_3^{\text{phys}} [Q_{\alpha,\beta}] \right] \right] = \sum_{\mathbf{j} \in \{0,1\}^3} (-1)^{|\mathbf{j}|} Q_{\alpha - \mathbf{j}, \beta};$$

$$\Delta^{\text{stoc}}[Q_{\alpha,\beta}] = \sum_{\mathbf{j} \in \{0,1\}^N} (-1)^{|\mathbf{j}|} Q_{\alpha, \beta - \mathbf{j}}.$$

The latter expressions are known in the sparse-grids community as “combination-technique” formulations, and can be very useful for practical implementations. In particular, they allow to evaluate e.g.  $\Delta^{\text{phys}}[Q_{\alpha,\beta}]$  by calling pre-existing softwares on different meshes up to  $2^3$  times in a “black-box” fashion. Analogously, evaluating  $\Delta^{\text{stoc}}[Q_{\alpha,\beta}]$  requires evaluating up to  $2^N$  operators  $Q_{\alpha,\beta}$  over different quadrature grids, and evaluating  $\Delta^{\text{mix}}[Q_{\alpha,\beta}]$  requires evaluating up to  $2^{3+N}$  operators  $Q_{\alpha,\beta}$  over different quadrature grids and physical meshes. Observe that by introducing these detail operators a hierarchical decomposition of  $Q_{\alpha,\beta}$  is available; indeed, the following is a telescopic identity

$$Q_{\alpha,\beta} = \sum_{[\mathbf{i}, \mathbf{j}] \leq [\alpha, \beta]} \Delta^{\text{mix}}[Q_{\mathbf{i}, \mathbf{j}}], \quad (3)$$

i.e., it can be easily verified by replacing each term  $\Delta^{\text{mix}}[Q_{i,j}]$  with the corresponding combination-technique formula that all terms except  $Q_{\alpha,\beta}$  will cancel. As an example, the case of one-dimensional physical and stochastic spaces can be considered. Recalling that by definition  $Q_{i,j} = 0$  when either  $i = 0$  or  $j = 0$ , it can be seen that

$$\begin{aligned} \sum_{[i,j] \leq [2,2]} \Delta^{\text{mix}}[Q_{i,j}] &= \Delta^{\text{mix}}[Q_{1,1}] + \Delta^{\text{mix}}[Q_{1,2}] + \Delta^{\text{mix}}[Q_{2,1}] + \Delta^{\text{mix}}[Q_{2,2}] \\ &= Q_{1,1} + (Q_{1,2} - Q_{1,1}) + (Q_{2,1} - Q_{1,1}) + Q_{2,2} - Q_{2,1} - Q_{1,2} - Q_{1,1} \\ &= Q_{2,2}. \end{aligned}$$

The crucial observation is that not all of the details in the above hierarchical decomposition (3) contribute equally to the approximation, i.e., they can be discarded and the resulting formula will retain good approximation properties at a fraction of the computational cost. Thus, the MISC approximation of  $\mathbb{E}[G_\alpha]$  is introduced as

$$\mathbb{E}[G_\alpha] \approx Q_\Lambda = \sum_{[\alpha,\beta] \in \Lambda} \Delta^{\text{mix}}[Q_{\alpha,\beta}],$$

for a suitable multi-index set  $\Lambda \subset \mathbb{N}^{3+N}$ , which should be chosen as downward closed, i.e. (see also Fig. 1a)

$$\forall \mathbf{k} \in \Lambda, \quad \mathbf{k} - \mathbf{e}_j \in \Lambda \text{ for every } j = 1, \dots, 3+N \text{ such that } \mathbf{k}_j > 1.$$

Clearly, the MISC estimator has a combination-technique expression as well, which can be written in compact form as

$$\mathbb{E}[G_\alpha] \approx Q_\Lambda = \sum_{[\alpha,\beta] \in \Lambda} \Delta^{\text{mix}}[Q_{\alpha,\beta}] = \sum_{[\alpha,\beta] \in \Lambda} \sum_{\substack{[i,j] \in \{0,1\}^{3+N} \\ [\alpha+i,\beta+j] \in \Lambda}} (-1)^{|[i,j]|} Q_{\alpha,\beta}, \quad (4)$$

which finally shows the initial statement that the MISC evaluation is computed by evaluating full-tensor operators  $Q_{\alpha,\beta}$  independently and combining them linearly according to (4). This is the approximation formula which is used in the practical implementation of the MISC method.

Of course, the effectiveness of the MISC estimator depends on the choice of the multi-index set  $\Lambda$ . Several strategies have been explored in the literature; a suitable set  $\Lambda$  can either be designed a-priori, by a careful analysis of the PDE at hand, see e.g. [13], or on-the-run by adaptive algorithms, see e.g. [14]; in this contribution the focus is on the latter option. To devise an optimal strategy for selecting a good multi-index set, the following error decomposition is introduced

$$\begin{aligned} |\mathbb{E}[G_\alpha] - Q_\Lambda| &= \left| \mathbb{E}[G_\alpha] - \sum_{[\alpha,\beta] \in \Lambda} \Delta^{\text{mix}}[Q_{\alpha,\beta}] \right| \\ &= \left| \sum_{[\alpha,\beta] \notin \Lambda} \Delta^{\text{mix}}[Q_{\alpha,\beta}] \right| \leq \sum_{[\alpha,\beta] \notin \Lambda} |\Delta^{\text{mix}}[Q_{\alpha,\beta}]| = \sum_{[\alpha,\beta] \notin \Lambda} E_{\alpha,\beta}, \end{aligned}$$

where  $E_{\alpha,\beta} := |\Delta^{\text{mix}}[Q_{\alpha,\beta}]|$ ;  $E_{\alpha,\beta}$  thus represents the “error contribution” of  $[\alpha,\beta]$ , i.e., the reduction in the approximation error due to having added  $[\alpha,\beta]$  to the current index-set  $\Lambda$ ; in formula

$$E_{\alpha,\beta} = |Q_{\Lambda \cup [\alpha,\beta]} - Q_\Lambda|. \quad (5)$$

Similarly, the “work contribution”  $W_{\alpha,\beta}$  is defined as the work required to add  $[\alpha,\beta]$  to the current index-set  $\Lambda$ . It is the product of the computational cost associated to the spatial grid identified by the multi-index  $\alpha$ , denoted by  $\text{cost}(\alpha)$  (see details in Sect. IV, Eq. 20), times the number of new evaluations of the PDE required by the multi-index  $\beta$ , i.e.

$$W_{\alpha,\beta} = \text{cost}(\alpha) \prod_{n=1}^N (m(\beta_n) - m(\beta_n - 1)) \quad (6)$$

with  $m$  defined as in (2). Note that the expression above is based on the fact that the employed quadrature rule is nested. An effective strategy to build adaptively a MISC approximation can then be broadly described as follows: given the MISC approximation associated to the multi-index set  $\Lambda$ , a new MISC approximation is built by adding to  $\Lambda$  the

multi-index with the next largest profit  $P_{\alpha,\beta} = \frac{E_{\alpha,\beta}}{W_{\alpha,\beta}}$ . Of course, it is impossible to compute in advance the profits of all multi-indices in  $\mathbb{N}^{3+N}$ , and it is required to guarantee that  $\Lambda$  is downward-closed at all times. Therefore, in practice the implementation reported in Algorithm 1 is used. It makes use of an auxiliary multi-index set, i.e. the margin of a multi-index set  $\Lambda$ ,  $\text{Mar}(\Lambda)$  which is defined as the set of multi-indices that can be reached “within one step” from  $\Lambda$  (see also Fig. 1b)

$$\text{Mar}(\Lambda) = \{\mathbf{i} \in \mathbb{N}^{3+N} \text{ s.t. } \mathbf{i} = \mathbf{j} + \mathbf{e}_k \text{ for some } \mathbf{j} \in \Lambda \text{ and some } k \in \{1, \dots, 3+N\}\}.$$

This algorithm was first proposed in the context of sparse-grids quadrature in [30] and its MISC implementation was first proposed in [14]. Note that the MISC method can also be used to obtain a surrogate model for  $G_\alpha(\mathbf{y})$ . More specifically, a formula analogous to (4) can be written replacing the tensor quadrature operator  $Q_{\alpha,\beta}$  by a tensor interpolation operator using global Lagrange polynomials collocated at the CC points, see e.g. [14]. The result is a linear combination of tensor interpolants according to the combination technique formula, which is used as surrogate response surface in Sect. IV. A further remark is that the choice of computing the profit based on the “improvement” of the approximation of the expected value of  $G$  is somehow arbitrary, and many alternatives can be considered, including interpolation-based versions, see e.g. [31–33] for the analogous discussion in the context of sparse-grids quadrature and interpolation.

Similarly, many stopping criteria can be considered (and possibly used simultaneously), which typically check that computational work, error contributions or profit estimator are below a desired threshold. More sophisticated error estimators are subject of research, see e.g. [34] in the context of sparse grids quadrature.

---

**Algorithm 1:** MISC implementation

---

**Multi-Index Stochastic Collocation**

```

I = {(1, 1)}, G = {(1, 1)}, RI = ∅;
Compute MISC estimate  $Q_G$  as in (4);
while stopping criteria are not met do
    for  $\mathbf{j} \in \text{Mar}(\mathbf{I})$  and  $\mathbf{I} \cup \{\mathbf{j}\}$  downward closed do // for short,  $\mathbf{j} = [\alpha, \beta]$ . See also Figure 1
        Compute MISC estimate  $Q_{G \cup \{\mathbf{j}\}}$  as in (4);
        Compute error contribution  $E_j$  as in (5);
        Compute work contribution  $W_j$  as in (6);
        Compute profit  $P_j = E_j / W_j$ ;
         $\mathbf{G} = \mathbf{G} \cup \{\mathbf{j}\}$ ,  $\mathbf{R}_I = \mathbf{R}_I \cup \{\mathbf{j}\}$ ;
    end
    Choose  $\mathbf{i} \in \mathbf{R}_I$  with the highest profit;
     $\mathbf{I} = \mathbf{I} \cup \{\mathbf{i}\}$ ,  $\mathbf{R}_I = \mathbf{R}_I \setminus \{\mathbf{i}\}$ ;
end
end

```

---

**B. Multi-Fidelity Stochastic Radial Basis Functions for numerical quadrature**

The methodology proposed here is based on the estimation of the quantities of interest by numerical quadrature applied to a multi-fidelity SRBF surrogate model. Given a training set  $\mathcal{T} = \{\mathbf{y}_i, G(\mathbf{y}_i)\}_{i=1}^J$  and normalizing the uncertain parameters domain into a unit hypercube, the RBF prediction is (here) based on a power function kernel and reads

$$f(\mathbf{y}, \tau) = \sum_{j=1}^{\mathcal{K}} w_j \|\mathbf{y} - \mathbf{c}_j\|^\tau, \quad (7)$$

where  $w_j$  are unknown coefficients,  $\mathbf{c}_j$  are the  $\mathcal{K}$  RBF centers, and  $\tau \sim \text{unif}[\tau_{\min}, \tau_{\max}]$  is a stochastic tuning parameter that follows a uniform distribution. RBF models have been widely applied in engineering problems using linear ( $\tau = 1$ , providing a polyharmonic spline of first order [35]) and cubic ( $\tau = 3$ , providing a polyharmonic spline of third order [36]) kernels. This suggests the range of  $\tau$  to be defined within  $\tau_{\min} = 1$  and  $\tau_{\max} = 3$ . Note that the choice of the distribution for  $\tau$  is arbitrary and, from a Bayesian viewpoint, this represents the degree of belief in the definition of the

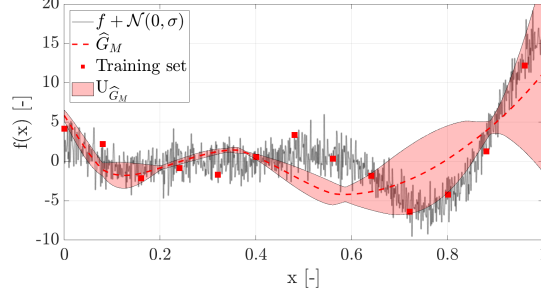


**Fig. 2 SRBF example with least-squares regression.**

tuning parameter. The SRBF prediction  $\tilde{G}(\mathbf{y})$  is computed as the expected value (approximated by MC) of  $f$  over  $\tau$  [37]:

$$\tilde{G}(\mathbf{y}) = \mathbb{E}[f(\mathbf{y}, \tau)]_{\tau} \approx \frac{1}{\Theta} \sum_{i=1}^{\Theta} f(\mathbf{y}, \tau_i), \quad (8)$$

where  $\Theta$  is the number of MC samples for  $\tau$ , here imposed equal to 1000.

Training data may or may not be affected by noise. Therefore, the coordinates of the RBF centers  $\mathbf{c}_j$  are not necessarily coincident with the training points, but defined via their k-means clustering [38] with an optimal number  $\mathcal{K}$  of centers defined by minimizing a leave-one-out cross-validation (LOOCV) metric [39]. In details, letting  $\tilde{g}(\mathbf{x})$  be a surrogate trained by the whole training set  $\mathcal{T}$  but the  $i$ -th training point,  $\mathcal{K}$  is defined as:

$$\mathcal{K} = \underset{\mathcal{K}_c \in C}{\operatorname{argmin}}(\operatorname{RMSE}), \quad (9)$$

where  $C \subset \mathbb{N}$  and the root mean squared error (RMSE) is

$$\operatorname{RMSE} = \sqrt{\frac{1}{\mathcal{J}} \sum_{i=1}^{\mathcal{J}} (G(\mathbf{y}_i) - \tilde{g}(\mathbf{y}_i))^2}. \quad (10)$$

Whenever the optimal number of RBF centers is lower than the training set size ( $\mathcal{K} < \mathcal{J}$ ), the coefficients  $w_j$  are determined through a least-squares regression by solving

$$\mathbf{w} = (\mathbf{A}^T \mathbf{A})^{-1} \mathbf{A}^T \mathbf{f}, \quad (11)$$

with  $\mathbf{w} = \{w_j\}$ ,  $a_{ij} = \|\mathbf{y}_i - \mathbf{c}_j\|^\tau$  and  $\mathbf{f} = \{G(\mathbf{y}_i)\}$ ; otherwise when the optimal number of RBF centers equals the training set size, exact interpolation at the training points ( $f(\mathbf{y}_i, \tau) = G(\mathbf{y}_i)$ ) is imposed and Eq. 11 reduces to

$$\mathbf{A} \mathbf{w} = \mathbf{f}, \quad (12)$$

with  $\mathbf{c}_j = \mathbf{y}_j$ . An example of least-squares regression is shown in Fig. 2.

The uncertainty  $U_{\tilde{G}}(\mathbf{y})$  associated with the SRBF prediction is quantified by the 95%-confidence band of the cumulative density function (CDF) of  $f(\mathbf{y}, \tau)$  as follows

$$U_{\tilde{G}}(\mathbf{y}) = \operatorname{CDF}^{-1}(0.975; \mathbf{y}) - \operatorname{CDF}^{-1}(0.025; \mathbf{y}), \quad (13)$$

with

$$\operatorname{CDF}(\lambda; \mathbf{y}) = \frac{1}{\Theta} \sum_{i=1}^{\Theta} H[\lambda - f(\mathbf{y}, \tau_i)], \quad (14)$$

where  $H(\cdot)$  is the Heaviside step function.

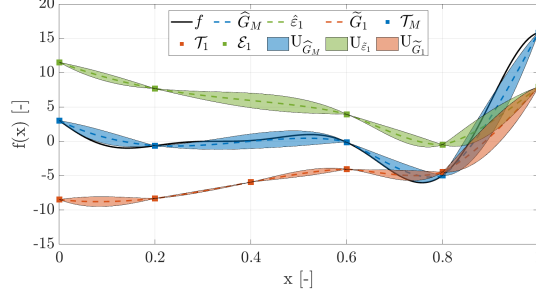


**Fig. 3** Example of multi-fidelity surrogate with  $M = 2$  and exact interpolation at the training points.

The multi-fidelity approximation, introduced in [40] and extended to noisy data in [41], is adaptively built as follows. Extending the definition of the surrogate training set to an arbitrary number of  $M$  fidelity levels as  $\{\mathcal{T}_\alpha\}_{\alpha=1}^M = \{\mathbf{y}_j, G_\alpha(\mathbf{y}_j)\}_{j=1}^{\mathcal{J}_\alpha}$ , the multi-fidelity approximation  $\hat{G}_\alpha(\mathbf{y})$  of  $G_\alpha(\mathbf{y})$  reads

$$\hat{G}_\alpha(\mathbf{y}) \approx \tilde{G}_1(\mathbf{y}) + \sum_{i=1}^{\alpha-1} \tilde{\varepsilon}_i(\mathbf{y}), \quad (15)$$

where  $\tilde{\varepsilon}_i(\mathbf{y})$  is the inter-level error surrogate with an associate training set  $\mathcal{E}_i = \{(\mathbf{y}, G_{i+1}(\mathbf{y}) - \hat{G}_i(\mathbf{y})) \mid \mathbf{y} \in \mathcal{T}_{i+1} \cap \mathcal{T}_i\}$ . It can be noted that Eq. 15 does not strictly require nested training sets. An example of the multi-fidelity approximation with two fidelities is shown in Fig. 3.

Assuming that the uncertainty associated to the prediction of the lowest-fidelity  $U_{\tilde{G}_1}$  and inter-level errors  $U_{\tilde{\varepsilon}_i}$  as uncorrelated, the multi-fidelity approximation  $\hat{G}_M(\mathbf{y})$  of  $G_M(\mathbf{y})$  and its uncertainty  $U_{\hat{G}_M}$  read

$$\hat{G}_M(\mathbf{y}) \approx \tilde{G}_1(\mathbf{y}) + \sum_{i=1}^{M-1} \tilde{\varepsilon}_i(\mathbf{y}) \quad \text{and} \quad U_{\hat{G}_M}(\mathbf{y}) = \sqrt{U_{\tilde{G}_1}^2(\mathbf{y}) + \sum_{i=1}^{M-1} U_{\tilde{\varepsilon}_i}^2(\mathbf{y})}. \quad (16)$$

Upon having evaluated  $U_{\hat{G}_M}$  the multi-fidelity surrogate is then updated adding a new training point following a two-steps procedure: firstly, the coordinates of the new training point  $\mathbf{y}^*$  are identified based on the SRBF maximum uncertainty [24], solving the single-objective maximization problem:

$$\mathbf{y}^* = \underset{\mathbf{y}}{\operatorname{argmax}} [U_{\hat{G}_M}(\mathbf{y})], \quad (17)$$

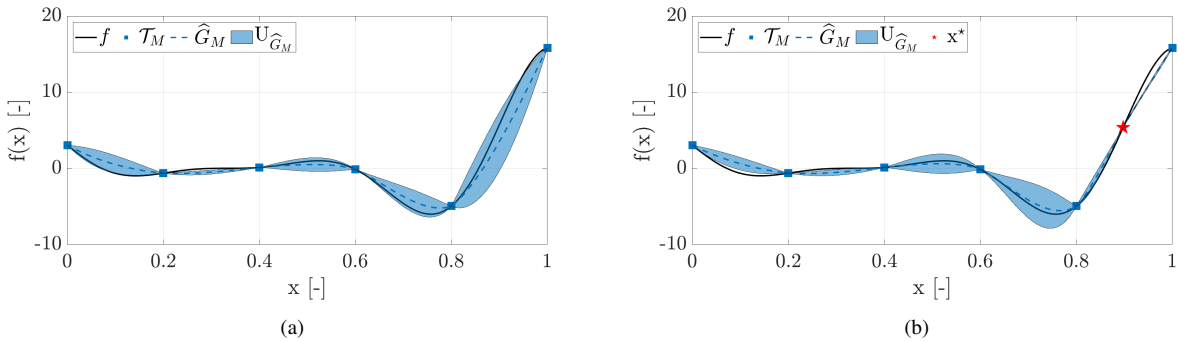


**Fig. 4** Example of the adaptive sampling method using one fidelity without noise: (a) shows the initial SRBF with the associated prediction uncertainty and training set; (b) shows the position of the new training point, the new SRBF prediction, and its uncertainty.



an example (with one fidelity only) is shown in Fig. 4. Secondly, once  $\mathbf{y}^*$  is identified, the training set/sets  $\mathcal{T}_\alpha$  are updated with a new training point  $\{\mathbf{y}^*, G_\alpha(\mathbf{y}^*)\}$  with  $\alpha = 1, \dots, k$ , where  $k$  is defined as

$$k = \text{maxloc} [\mathbf{U}(\mathbf{y}^*)] \quad \text{and} \quad \mathbf{U}(\mathbf{y}^*) \equiv \{U_{\tilde{G}_1}(\mathbf{y}^*)/\gamma_1, U_{\tilde{E}_1}(\mathbf{y}^*)/\gamma_2, \dots, U_{\tilde{E}_{M-1}}(\mathbf{y}^*)/\gamma_M\}. \quad (18)$$

where  $\gamma_\alpha$  is the computational cost associated to the  $\alpha$ -th level.

In the present work, the adaptive sampling procedure starts with five training points (for each fidelity level) located at the domain center and at the lower and upper bounds of each uncertain parameter. SRBF with exact interpolation is enforced for the  $\alpha$ -th fidelity level until  $\mathcal{J}_\alpha < 5^N$ , then the least-squares approximation is used. This because with such a low number of (distant) training points the exact interpolation generally provides a better approximation of the quantity of interest than the regression. Moreover, the presence of numerical noise of the quantity of interest can not be assessed with few training points, making the regression not useful at the initial stage of the adaptive sampling procedure. Once the least-squares approximation is used, the noise associated to  $\alpha$ -th fidelity/training set is assessed by Eq. 10 and then normalizing by the range of  $G_M$  (to this end, we consider the estimate of the range obtained by the evaluations of  $G_M$

---

**Algorithm 2:** Adaptive multi-fidelity SRBF implementation

---

**Multi-Fidelity SRBF for numerical quadrature**

```

Define the initial training set  $\{\mathcal{T}_\alpha\}_{\alpha=1}^M = \{\mathbf{y}_j, G_\alpha(\mathbf{y}_j)\}_{j=1}^{\mathcal{J}_\alpha}$ ;
while stopping criteria are not met do // iterate the adaptive sampling process with index  $t$ 
    Set  $\mathcal{K}_\alpha^t = \mathcal{J}_\alpha^t \forall \alpha$ ;
    for  $\alpha = 1, \dots, M$  do
        if  $\mathcal{J}_\alpha^t > 5^N$  then // SRBF auto-tuning based on LOOCV
            Find  $\mathcal{K}_\alpha^t$  as in Eq. (9) with  $C = [\mathcal{K}^{t-1}, \mathcal{J}^t]$ ;
        end
    end
    Construct the SRBF surrogate  $\hat{G}_1(\mathbf{y})$  as in Eq. (8); // low-fidelity approximation
    Compute the prediction uncertainty  $U_{\hat{G}_1}(\mathbf{y})$  as in Eq. (13);
    for  $\alpha = 2, \dots, M-1$  do // evaluate surrogates of the inter-level errors
        Compute the inter-level errors;
        Construct the SRBF surrogates of the inter-level errors  $\tilde{E}_\alpha$  as in Eq. (8);
        Compute the prediction uncertainty  $U_{\tilde{E}_\alpha}$  as in Eq. (13);
    end
    Construct the multi-fidelity approximation  $\hat{G}_M(\mathbf{y})$  as in Eq. (16); // MF approximation
    Compute the multi-fidelity prediction uncertainty  $U_{\hat{G}_M}$  as in Eq. (16);
    for  $j = 1, \dots, p$  do // perform parallel infill
        Find  $\mathbf{y}^* = \underset{\mathbf{y}}{\text{argmax}}[U_{\hat{G}_M}(\mathbf{y})]$ ;
        Find  $k_j = \text{maxloc} [\mathbf{U}(\mathbf{y}^*)]$  as in Eq. (18);
        Update the training sets  $\{\mathcal{T}_\alpha\}_{\alpha=1}^{k_j} \cup \{\mathbf{y}^*, \hat{G}_\alpha(\mathbf{y}^*)\}_{\alpha=1}^{k_j}$ ; // considering exact prediction
        Update the training sets size  $\{\mathcal{J}_\alpha^{t+j}\}_{\alpha=1}^{k_j} = \{\mathcal{J}_\alpha^t\}_{\alpha=1}^{k_j} + 1$ ;
    end
    for  $j = 1, \dots, p$  do // perform new simulations
        Evaluate  $\{\mathbf{y}_j^*, G_\alpha(\mathbf{y}_j^*)\}_{\alpha=1}^{k_j}$ ;
        Update the training sets  $\{\mathcal{T}_\alpha\}_{\alpha=1}^{k_j} \cup \{\mathbf{y}^*, G_\alpha(\mathbf{y}^*)\}_{\alpha=1}^{k_j}$ ;
        Update the training sets size  $\{\mathcal{J}_\alpha^{t+j}\}_{\alpha=1}^{k_j} = \{\mathcal{J}_\alpha^t\}_{\alpha=1}^{k_j} + 1$ ;
    end
    Evaluate the quantities of interest over the surrogate by numerical quadrature; // UQ
     $t = t + 1$ ; // Move to the next adaptive sampling iteration
end
end

```

---

available after the first iteration). Furthermore, to avoid abrupt changes in the SRBF prediction (when regression is used) from one iteration to the next one, the search for the optimal  $\mathcal{K}$  can be constrained. Herein, defining  $t$  as the adaptive sampling iteration, the problem in Eq. 9 is solved assuming  $C = [\mathcal{K}^{t-1}, \mathcal{J}^t]$ , with  $\mathcal{J}^t$  the training set size at the  $t$ -th iteration, except for the first iteration with least-squares approximation, where no constraint is imposed.

A deterministic version of the particle swarm optimization algorithm [42] is used for the solution of the optimization problem in Eq. 17.

Since the numerical simulations can be performed with an hardware capable of running  $p$  simulations simultaneously, a parallel-infill approach is used in combination with the adaptive sampling method. In the present work, four training points were added to the training sets at each adaptive sampling iteration. The parallel-infill approach computes four sub-iterations for each  $t$ -th iteration. In each sub-iteration  $j$ , the training point  $\mathbf{y}_j^*$  is identified by Eq. 18 and the SRBF prediction  $\hat{G}_\alpha(\mathbf{y}_j^*)$  is added to the  $\alpha$ -th training set, assuming the SRBF prediction as exact prediction. Once the four training point are identified, the actual simulations are performed and the corresponding outputs are used to update the training sets. Details of the SRBF adaptive sapling procedure are described in Algorithm 2.

Finally, numerical quadrature is used on the SRBF surrogate model to estimate the expected value of the quantity of interest  $\mathbb{E}[\hat{G}_M]$ . Herein, Eq. 1 is estimated following the midpoint rule, with a full-factorial sampling over the SRBF prediction with  $S = 100^N$  samples, as

$$\mathbb{E}[G_M] \approx \mathbb{E}[\hat{G}_M] \approx \frac{1}{S} \sum_{j=1}^S \hat{G}_M(\mathbf{y}_j). \quad (19)$$

### III. Problem Formulation and CFD Method

The problem addressed in this manuscript is the forward UQ analysis of the model-scale resistance ( $R_T$ ) of a RoPax ferry in straight ahead advancement, subject to two operational uncertainties  $\mathbf{y} = [U, T]$ , namely the advancement speed ( $U$ ) and the draught ( $T$ ), uniformly distributed within the ranges in Tab. 1.

The RoPax ferry is characterized by a length between perpendicular at nominal draught ( $L_{PP}$ ) of 162.85 m and a block coefficient  $C_B = 0.5677$  (see Fig. 5). The parametric geometry of the RoPax is produced with the computer-aided design environment integrated in the CAESSES<sup>®</sup> software, developed by FRIENDSHIP SYSTEMS AG, and made available in the framework of the H2020 EU Project Holiship. The analysis is performed at model scale with a scale factor equal to 27.14. The main dimensions and the operative conditions are summarized in Tab. 1. The advancement speed ranges from 12 to 26 knots at full scale and the draught variation is  $\pm 10\%$  of the nominal draught, which corresponds to a variation of about  $\pm 15\%$  of the nominal displacement. The corresponding range in Froude number  $Fr = U/\sqrt{gL_{PP}}$  is  $[0.154, 0.335]$ , whereas the variation in Reynolds number (at model scale)  $Re = \rho UL_{PP}/\mu = UL_{PP}/\nu$  is  $[6.423 \cdot 10^6, 1.392 \cdot 10^7]$ , where  $\rho = 998.2 \text{ kg/m}^3$  is the water density,  $\nu = \mu/\rho = 1.105 \cdot 10^{-6} \text{ m}^2/\text{s}$  the kinematic viscosity and  $g = 9.81 \text{ m/s}^2$  the gravitational acceleration.

The hydrodynamics performance of the RoPax ferry is assessed by the RANS code  $\chi$ navis developed at CNR-INM [26–28]. It is based on a finite volume scheme, with variables collocated at the cell centers. Turbulent stresses are taken into account by the Boussinesq hypothesis, with the Spalart-Allmaras turbulence model. Free-surface effects are taken into account by a single-phase level-set algorithm. Wall-functions are not adopted, therefore the wall distance  $y^+ = 1$  is ensured on the wall.

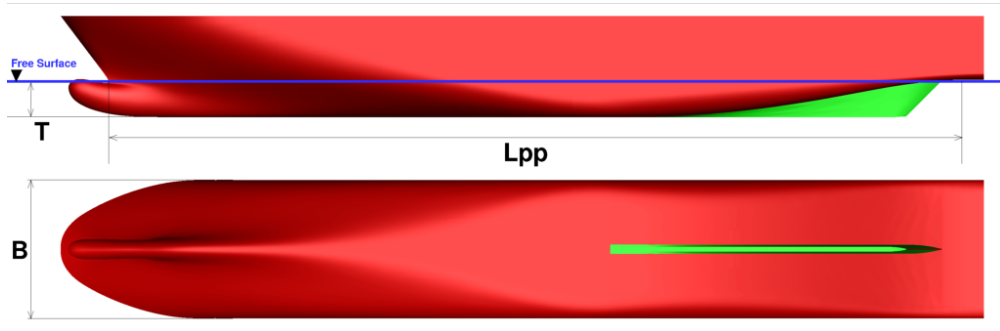
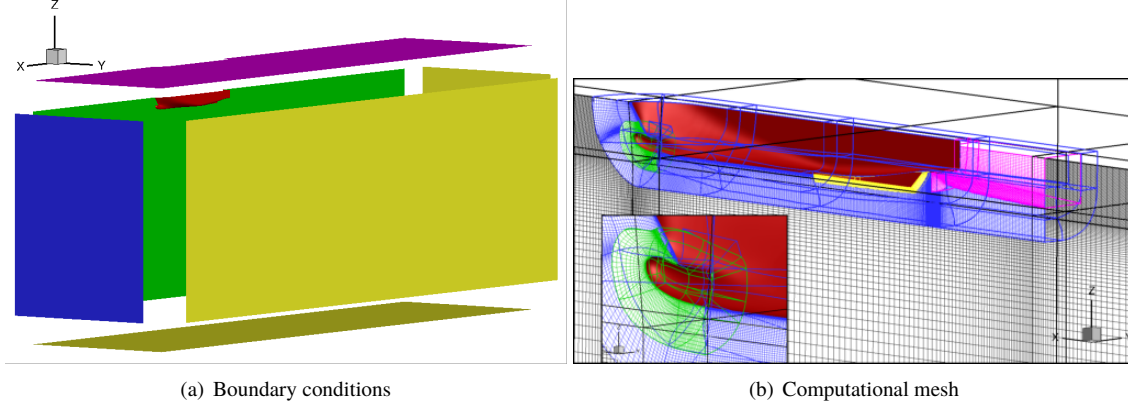


Fig. 5 RoPax ferry: hull form.



**Fig. 6 Numerical setup: boundary conditions and computational grid.**

The computational domain extends to  $2L_{pp}$  in front of the hull,  $3L_{pp}$  behind, and  $1.5L_{pp}$  each side; a depth of  $2L_{pp}$  is imposed (see Fig. 6). On the solid walls (in red in the figure), the velocity is set equal to zero, whereas zero normal gradient is enforced on the pressure field; at the (fictitious) inflow boundary (blue), the velocity is set to the undisturbed flow value and the pressure is extrapolated from inside; the dynamic pressure is set to zero at the outflow (yellow), whereas the velocity is extrapolated from inner points. On the top boundary, which remains always in the air region, fluid dynamic quantities are extrapolated from inside (purple). Taking advantage of the symmetry of the flow relative to the  $y = 0$  plane, computations are performed for half ship only, usual symmetry boundary conditions are enforced on the symmetry longitudinal plane (in green in Fig. 6a).

The computational grid is composed by 60 adjacent and partially overlapped blocks; Fig. 6b shows a particular of the block structures in the region around the ship hull and the computational mesh on the symmetry plane. Taking the advantage of a Chimera overlapping approach, the meshes around the skeg and around the bow are generated separately from the mesh around the hull; a background Cartesian grid is then built and the whole grid is assembled by means of an in-house overlapping grid pre-processor. The final mesh counts for a total of about 5.5M of control volumes for half the domain. The numerical solutions are computed by means of a full multi-grid–full approximation scheme (FMG–FAS), with four grid levels (from coarser to finer:  $M_1$ ,  $M_2$ ,  $M_3$ , and  $M_4$ ), each obtained from the next finer grid with a coarsening ratio equal to 2, along each curvilinear direction. In the FMG–FAS approximation procedure, the solution is computed on the coarsest grid level first. Secondly, it is approximated on the next finer grid and the solution is iterated by exploiting all the coarser grid levels available with a V-Cycle. The process is repeated up to the finest grid level. For the present UQ problem all the four grid levels are used; to note, the number of grid volumes ranges from 5.5M for the finest mesh, down to 11K for the coarsest one. To provide an idea about the different mesh resolution between the grid

**Table 1 Main geometrical details and operative conditions of the RoPax ferry (model scale 1 : 27.14).**

Description	Symbol	Full Scale	Model Scale	Unit
Length between perpendiculars	$L_{pp}$	162.85	6.0	m
Beam	$B$	29.84	1.0993	m
Block coefficient	$C_B$	0.5677	0.5677	–
Nominal displacement	$\nabla$	19584.04	0.9996	m <sup>3</sup>
Nominal draught	$T_n$	7.10	0.261660	m
Draught range	$T$	[7.812, 6.391]	[0.2355, 0.2878]	m
Speed range	$U$	[6.173, 13.376]	[1.185, 2.567]	m/s
Froude range	Fr	[0.154, 0.335]	[0.154, 0.335]	–
Reynolds range	Re	$[9.081 \cdot 10^8, 1.968 \cdot 10^9]$	$[6.423 \cdot 10^6, 1.392 \cdot 10^7]$	–

levels, Fig. 7 shows a particular of the grid at the bow region for  $\mathcal{M}_3$ ,  $\mathcal{M}_2$  and  $\mathcal{M}_1$  grids ( $\mathcal{M}_4$  is in the insert of Fig. 6b).

Based on the grid refinement ratio chosen, a normalized computational cost for the  $\alpha$ -th grid level can be estimated as:

$$\text{cost}(\alpha) = 8^{\alpha-1} \quad (20)$$

with  $\alpha = 1, \dots, 4$ . In the FMG-FAS scheme the computation on the  $\alpha$ -th grid level involves computations on all the coarser meshes  $\mathcal{M}_1 \dots \mathcal{M}_{\alpha-1}$ . However, with the estimation in Eq. 20, only the cost of the highest-fidelity level samples is taken into account, i.e. the computations on the coarser grids are considered negligible.

Fig. 8 shows an overview of the numerical solutions obtained for different conditions in terms of wave pattern

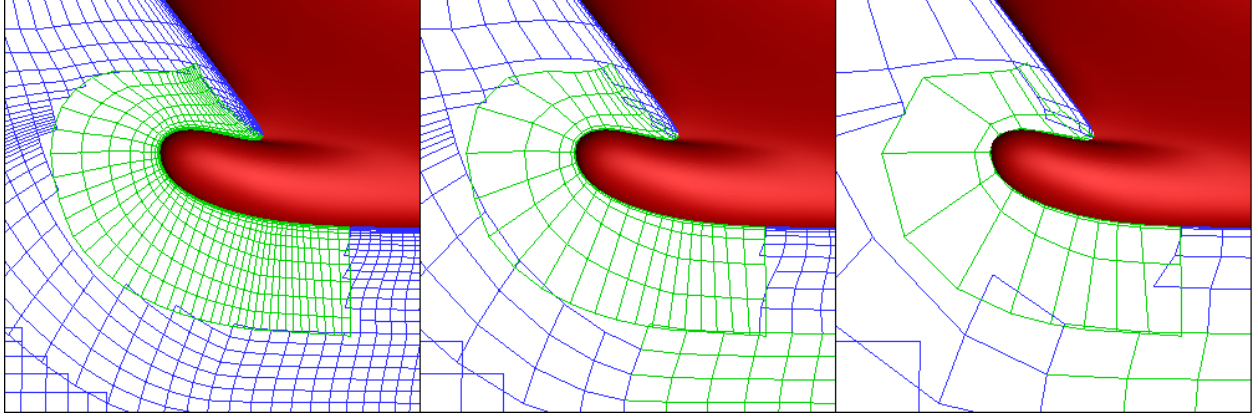


**Fig. 7** RoPax grids: detail of the bow region, left to right:  $\mathcal{M}_3$  (699k),  $\mathcal{M}_2$  (87k),  $\mathcal{M}_1$  (11k).

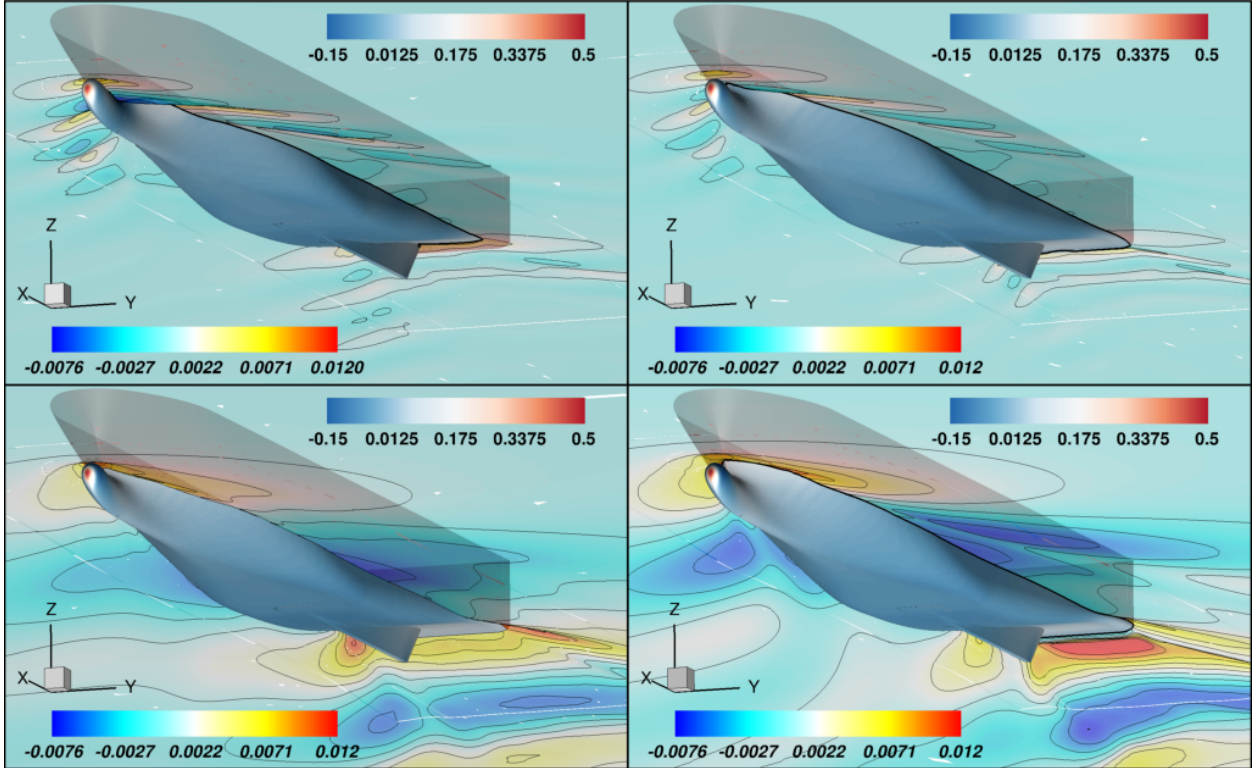


**Fig. 8** RoPax ferry,  $\mathcal{M}_4$  CFD results in terms of non-dimensional wave pattern and surface pressure for:  $\text{Fr} = 0.193$ ,  $T = 3.9249 \cdot 10^{-2} L_{PP}$  and  $T = 4.7971 \cdot 10^{-2} L_{PP}$ , top row left and right;  $\text{Fr} = 0.335$ ,  $T = 3.9249 \cdot 10^{-2} L_{PP}$  and  $T = 4.7971 \cdot 10^{-2} L_{PP}$ , bottom row left and right.

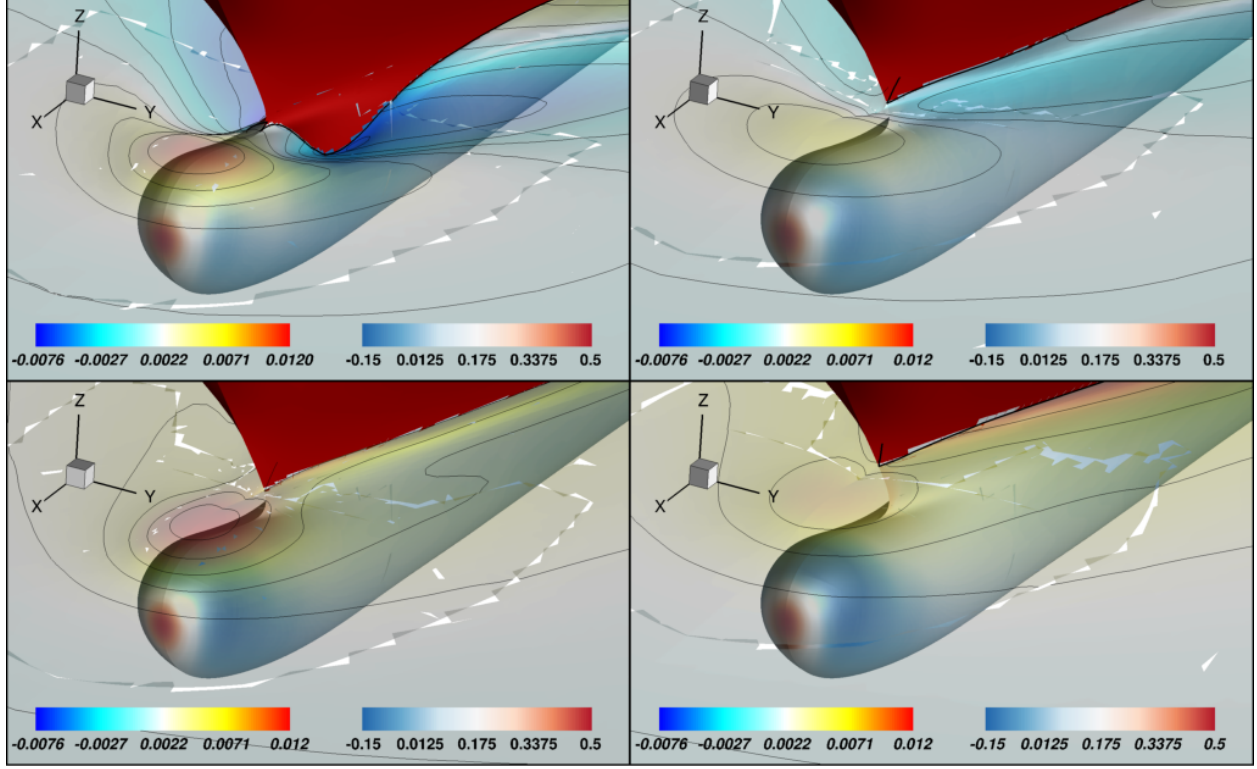


**Fig. 9** RoPax ferry, enlarged view of the bow region as in Fig. 8.

and hull surface; wave height (as elevation with respect to the unperturbed level) and surface pressure are reported in non-dimensional values, making the height non dimensional with  $L_{PP}$  and the pressure with  $\rho U^2 L_{PP}^2$ , as usual. A clear, and obvious, Froude number dependency is seen for the wave patterns; at the lower speed shown, the free surface is weakly perturbed (to note, the same color range has been used for all the panels), whereas, at higher Froude, a clear kelvin pattern is seen. Also, at higher speed, the formation of a well defined transom wave system is observed, including the presence of the classical rooster tail. It is also worth to observe the influence of the draught on the wave system; in particular at the lower speed reported, and the smaller draught, the rear part of the bulbous is partially dry (better seen in the enlarged views reported in Fig. 9). The region of very low pressure, caused by the flow acceleration around the bow, is obviously the cause. For all cases, the high pressure in the stagnation point at the bow prevents the bow to be outside the water, as it is at the rest conditions at least for the nominal and the smaller draughts (see Fig. 5). For higher speed, the larger draught condition causes a stronger rooster tail system at the stern, with higher crest and trough.

#### IV. Numerical Results

In this section the behavior of the two methods applied to the problem just described is illustrated. To fairly compare the outcomes of the two UQ methodologies presented, no termination criteria are used for both methods, that are stopped when sufficient and comparable computational costs have been reached.

Fig. 10 shows the convergence of the expected value and standard deviation of  $R_T$  versus the computational cost. MISC and SRBF converge towards similar estimates. MISC achieves good estimate already with low computational cost, whereas at later iterations, corresponding to computational cost above 1000, its behavior worsens; conversely SRBF gives a more stable estimate. Similar conclusions can be drawn by looking at the plot of the values of the standard deviation. Complementary information are given in Tab. 2, summarizing the expected value and the standard deviation achieved by the two methods at the final iteration and at one characteristic iteration. In the case of MISC iteration 14 (associated to a computational cost equals to 900) is selected, one of the iterations giving a good estimate of the expected value but before the “disruption” happening around cost approximately 1000. Such iteration is indicative of the behavior of MISC and the successive discussions are referred to it. Concerning SRBF, the convergence of the expected



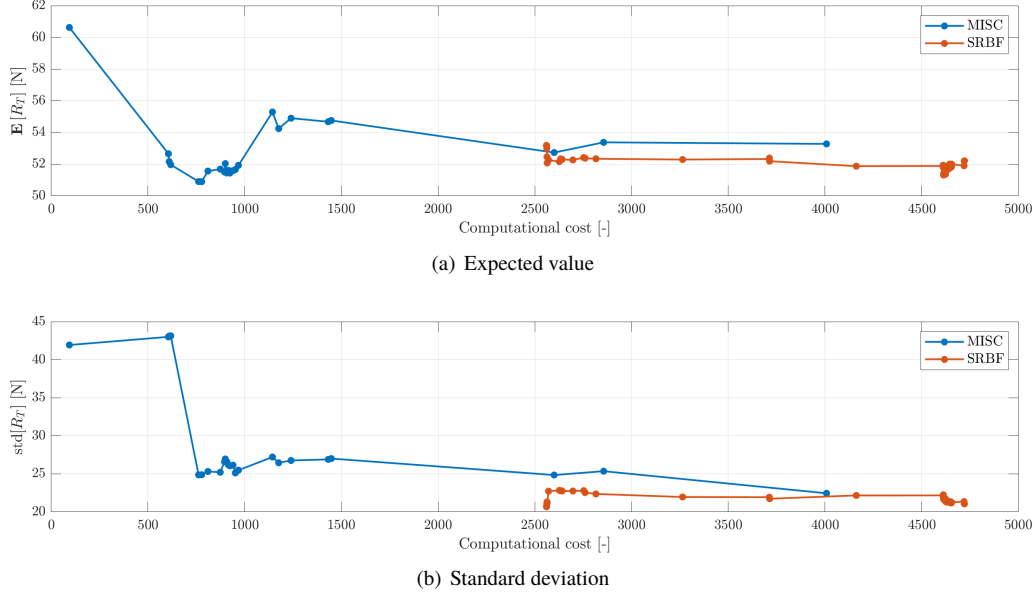


**Fig. 10 Comparison of MISC and SRBF results: convergence of the expected value and standard deviation of  $R_T$  versus computational cost. For the sake of readability, we plot the results for MISC starting with the 4th iteration. The first three iterations correspond to computational cost 1, 12, and 14, and give poor results.**

value and the standard deviation is oscillatory (zoom not shown for brevity). The oscillation becomes more evident after iteration 8 with computational cost of 4638, which is then selected as characteristic iteration for the SRBF and shown in Tab. 2). Actually, after this iteration the SRBF moves from interpolation to least-squares approximation for the lowest fidelity only, since its number of training points reaches the threshold value of  $5^N$ . This produces oscillations in the last part of the SRBF convergence. Nevertheless, variations are small and oscillations limited.

Fig. 11 shows the  $R_T$  histogram and its kernel density estimation. The PDF obtained with SRBF has a peak around in the interval 20-40. A similar peak is retrieved also by MISC. However, in the latter case secondary peaks are observed for higher values of resistance at the final iteration. SRBF with exact interpolation (see Fig. 11c) leads to a peak value significantly higher than MISC and SRBF with least-squares regression (see Fig. 11a, b, and d).

Total resistance response surfaces are shown and compared in Fig. 12. Once again, it can be observed that the behavior of MISC deteriorates at later iterations. The response surface is very irregular and this can be attributed to the numerical noise which affects the CFD simulations, in particular the one on the coarsest grid. As the overall idea of MISC is to solve most PDEs on the less expensive grids and building the surrogate model with lagrangian (hence exact) interpolation, the presence of numerical noise turns out to be problematic for this method. This issue could be mitigated by doing e.g. a least-squares regression on the data, to smooth the numerical oscillations. A more thorough investigation of this aspect is out of scope here and will be considered in a future work (see also discussion in Sect. V - Conclusions). On the contrary, SRBF suffers the numerical noise of the CFD outputs till the exact interpolation is

**Table 2 Comparison of MISC and SRBF results: computational cost, expected value and standard deviation of  $R_T$  for an intermediate iteration and at the final iteration.**

UQ method	MISC		SRBF	
Iteration	14	final	8	final
Computational cost	900	4008	4638	4721
$\mathbb{E}[R_T]$	52.0	53.3	51.7	52.2
$\text{std}[R_T]$	26.9	22.4	21.4	21.0

imposed (see Fig. 12c) leading to a significant deformation of the response surface close to the lower bound of both the uncertain parameters), whereas increasing the iteration (and the computational cost) the use of regression improves the quality of the surrogates by smoothing the response surface and filtering out the numerical noise (see Fig. 12d).

Fig. 13 displays the points in the uncertain parameter space selected by MISC and SRBF. The two plots on the top line show the points employed by MISC at iteration 14 and at the final iteration. At the beginning the MISC algorithm explores more in advancement speed direction, suggesting a stronger dependence of the quantity of interest on the advancement speed rather than on the draught. Points exploring the direction of the draught are added only at later iterations (this subject is elaborated also later on). The sampling performed by SRBF is shown in Figs. 13c and Figs. 13d at 8 and final iteration, respectively. Until iteration 8 (exact interpolation only), the adaptive sampling method explores the domain extrema and starts to cluster samples in two zones among  $U = [7, 8.8]$  m/s, since the numerical noise negatively affects the prediction uncertainty of the interpolating SRBF. Switching to the least-squares approximation and filtering out the noise prevents an excessive clusterization of the samples at the successive iterations.

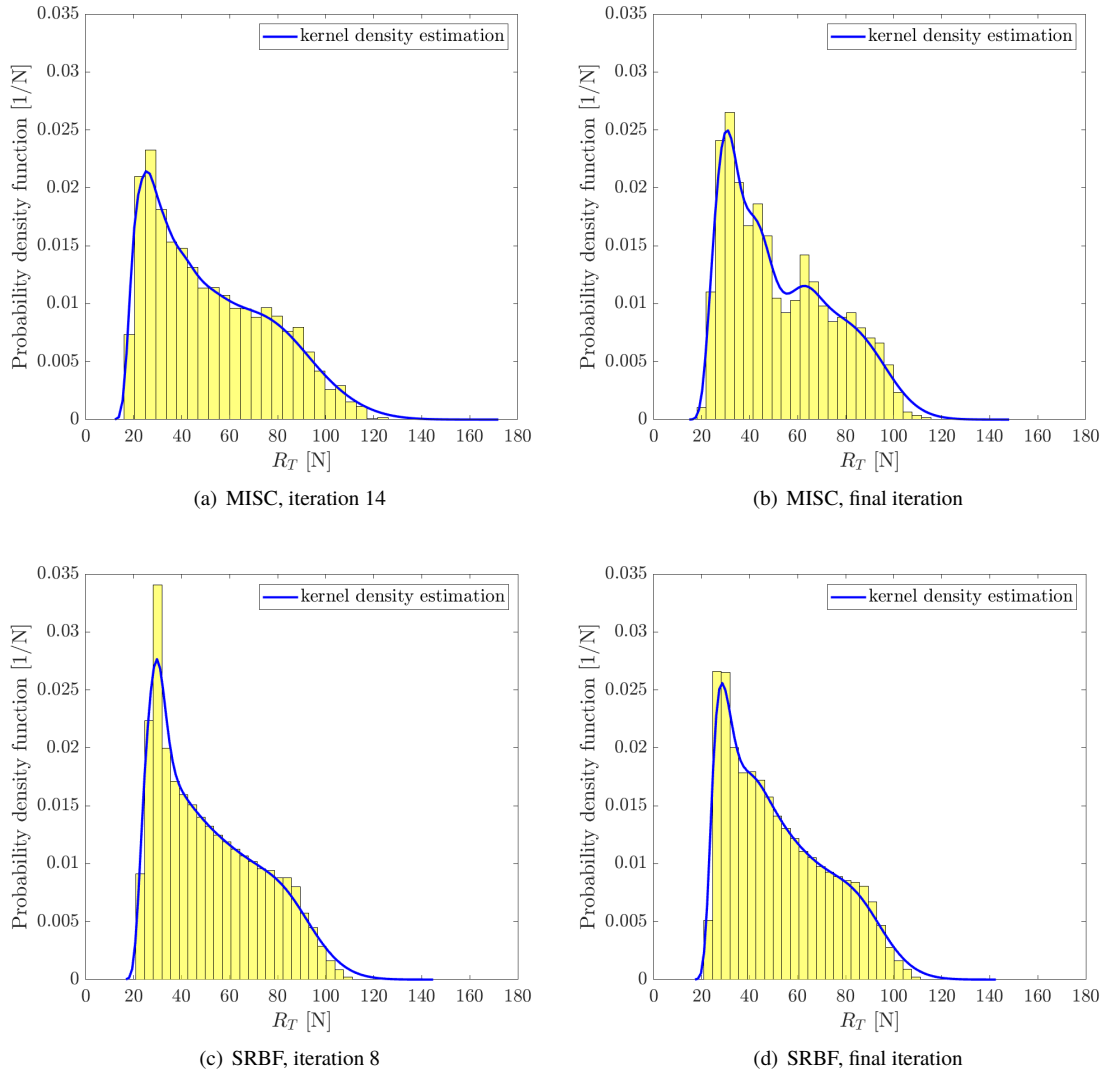


**Fig. 11 Comparison of MISC and SRBF results: density function and histogram of (rescaled) frequencies of  $R_T$ . The histogram is computed using 25 bins for  $n = 10000$  samples of the response surface. The probability density function is estimated using the kernel smoothing estimate given by the Matlab's `ksdensity` function, enforcing positive support and with automatic selection of the bandwidth.**

Indeed, the SRBF samples are fairly spread over the domain.

Fig. 14 shows the amount of simulations on the different spatial grids required by both methods at each iteration. Specifically, on the left the total number of simulations is displayed, whereas on the right only the number of new simulations asked at each iteration is shown. MISC required most of the simulations on the coarse grid; only five simulations on the finest grid are required (one at iteration 5, two at iteration 28, and two at iteration 30). At iteration 12, 24, and 25 no new points are added, which can be explained as follows. At iteration 12 the MISC algorithm requires simulations for spatial index  $\alpha = 5$ : however, having considered only four spatial refinements level, this grid was not available. The profit of this multi-index is then set to zero and the algorithm restarts to explore from the multi-index with the next highest profit. Instead, at iteration 24 and 25 there is no new index  $\mathbf{j}$  to be added to the multi-index set because

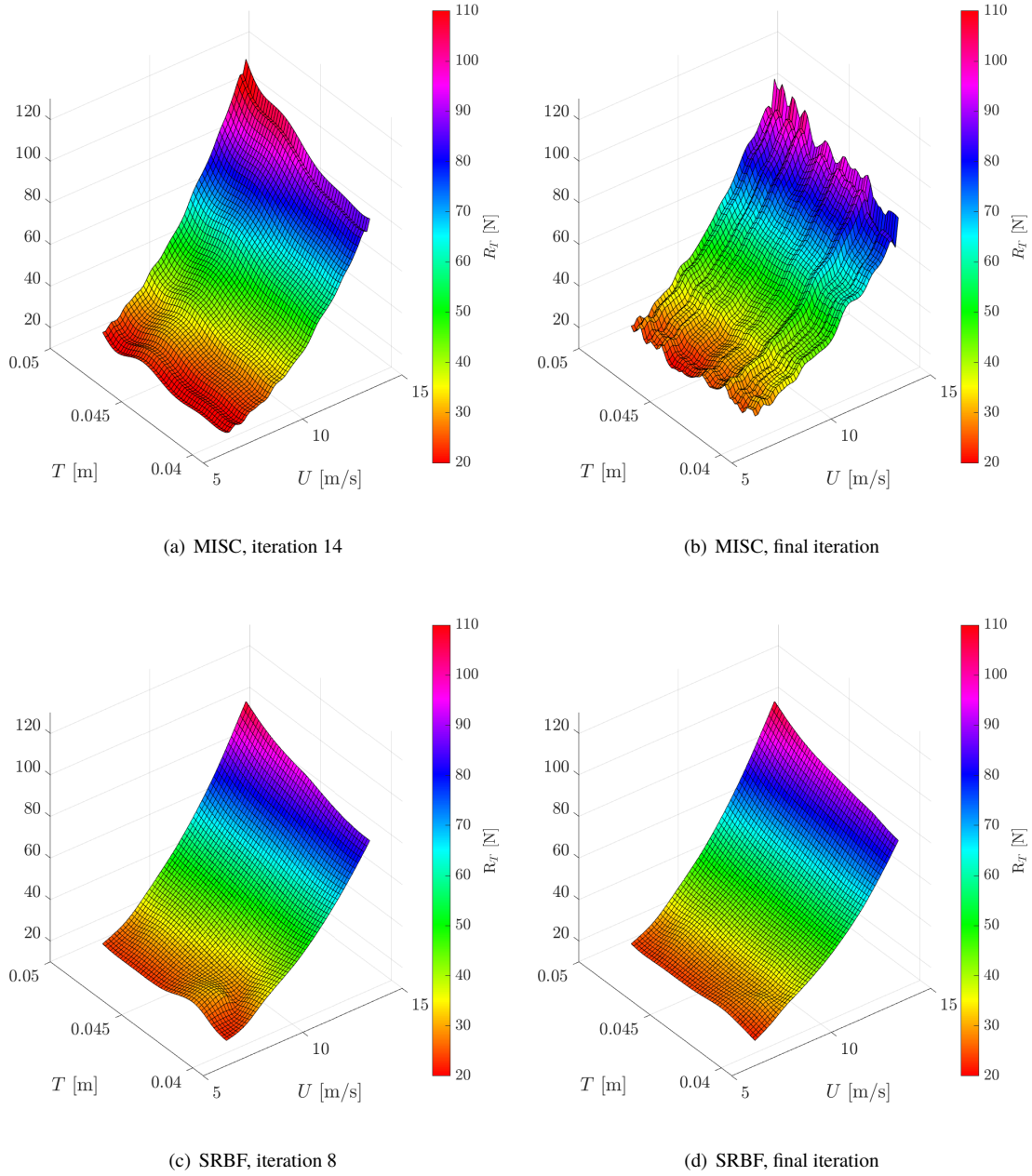


**Fig. 12 Comparison of MISC and SRBF results: response surfaces.**



none of the indices  $\mathbf{j} \in \text{Mar}(\mathbf{I})$  would lead to  $\mathbf{I} \cup \{\mathbf{j}\}$  downward closed, see Algorithm 1. As for SRBF, it spend about 50% of the final computational cost at the first iteration, then requiring simulations on the finest grids only at iterations 5 and 6. In all the other iterations mainly low-fidelity simulations are performed. This sampling behavior is due to the high values of prediction uncertainty that are found in the corners of the variables domain, because the topology of the initial training leads to extrapolation in those zones. Such corner regions are those with the highest estimated prediction uncertainty, and the adaptive sampling procedure requires all the fidelities before moving to explore other regions.

Fig. 15a shows the maximum prediction uncertainty versus the computational cost. After the first four iterations the value of the maximum prediction uncertainty decreases from 120% of the high-fidelity function range ( $R_1$ ) to about 25%. During the adaptive sampling the value of the maximum prediction uncertainty continues to decrease slower than in the first iterations, achieving a final value of about 5%. The convergence shows some oscillations around a computational cost equal to 4600, due to the change from exact interpolation to least-squares approximation of the training set. Fig. 15b compares the convergence of the maximum prediction uncertainty with its low-fidelity component and the normalized (with the function range) RMSE of the lowest-fidelity training set from iteration 8. It is worth noting that the lowest-fidelity prediction uncertainty is almost equal to the maximum multi-fidelity prediction uncertainty until

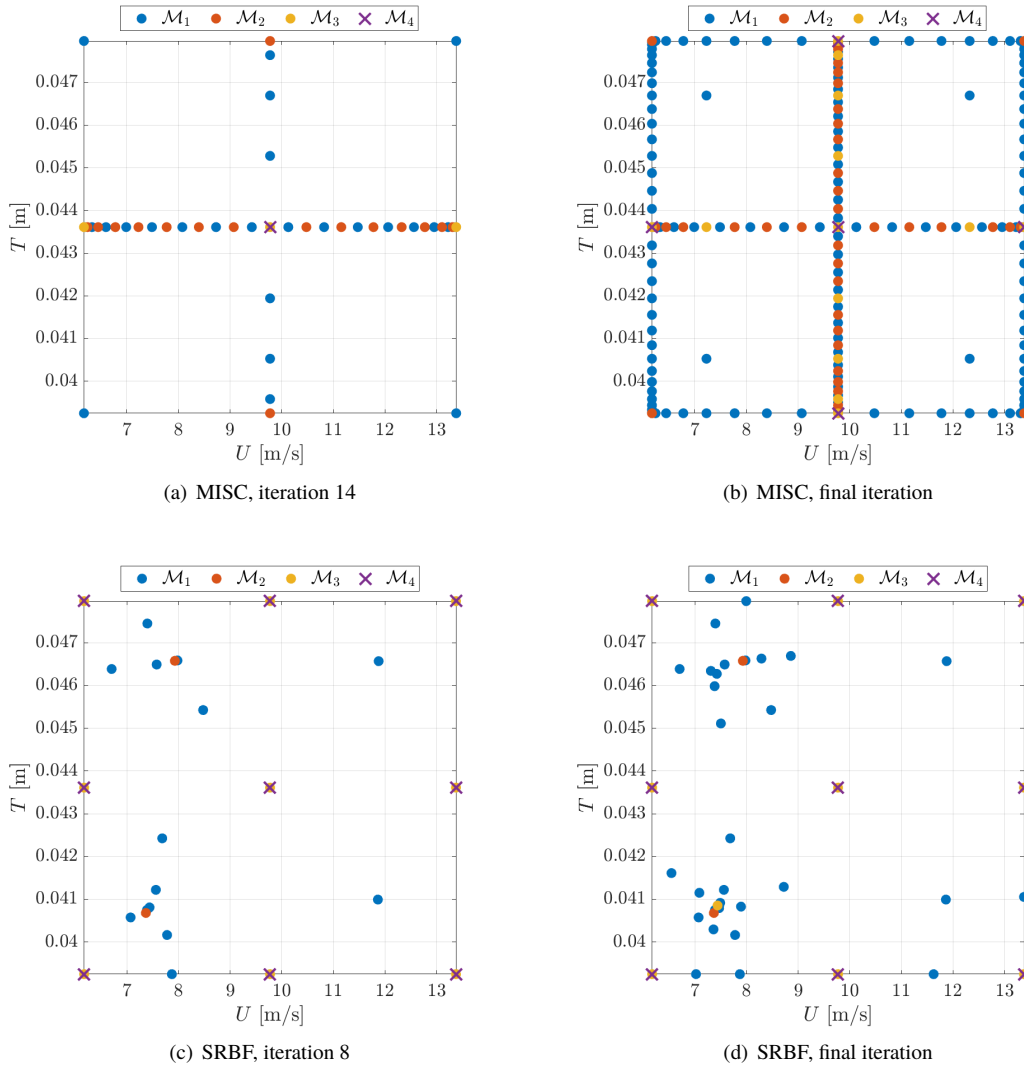


**Fig. 13 Comparison of MISC and SRBF results: points in parameter space. Note that every point required on grid  $\mathcal{M}_i$  is required also on all the grids with lower refinement level.**

a computational cost of about 4655, thus representing its main component.

Finally, coming back to the analysis of the MISC results, in Fig. 16 the multi-indices  $[\alpha, \beta_1, \beta_2]$  selected by the MISC method until iteration 14 and at the final iteration are shown. It can be seen that the multi-index set at iteration 14 stretches more in direction “advancement speed” than in direction “draught”: this further confirms the statement already made that the parameter advancement speed is deemed more influential by MISC, i.e. the multi-indices with larger profits are predominantly found in direction advancement speed. More quantitative information on the profits can be found in Fig. 17, where the profit of every explored multi-index is displayed. Note that only the indices with the highest profits (marked in yellow) are added to the multi-index set  $I$ . The remaining indices are explored (i.e. added to the multi-index set  $G$ , therefore contribute to the MISC approximation) but non yet selected (i.e. added to the multi-index set  $I$ ). As already explained earlier on, there is no profit associated to the multi-index  $[5, 1, 1]$  since the fifth spatial refinements level is not available.

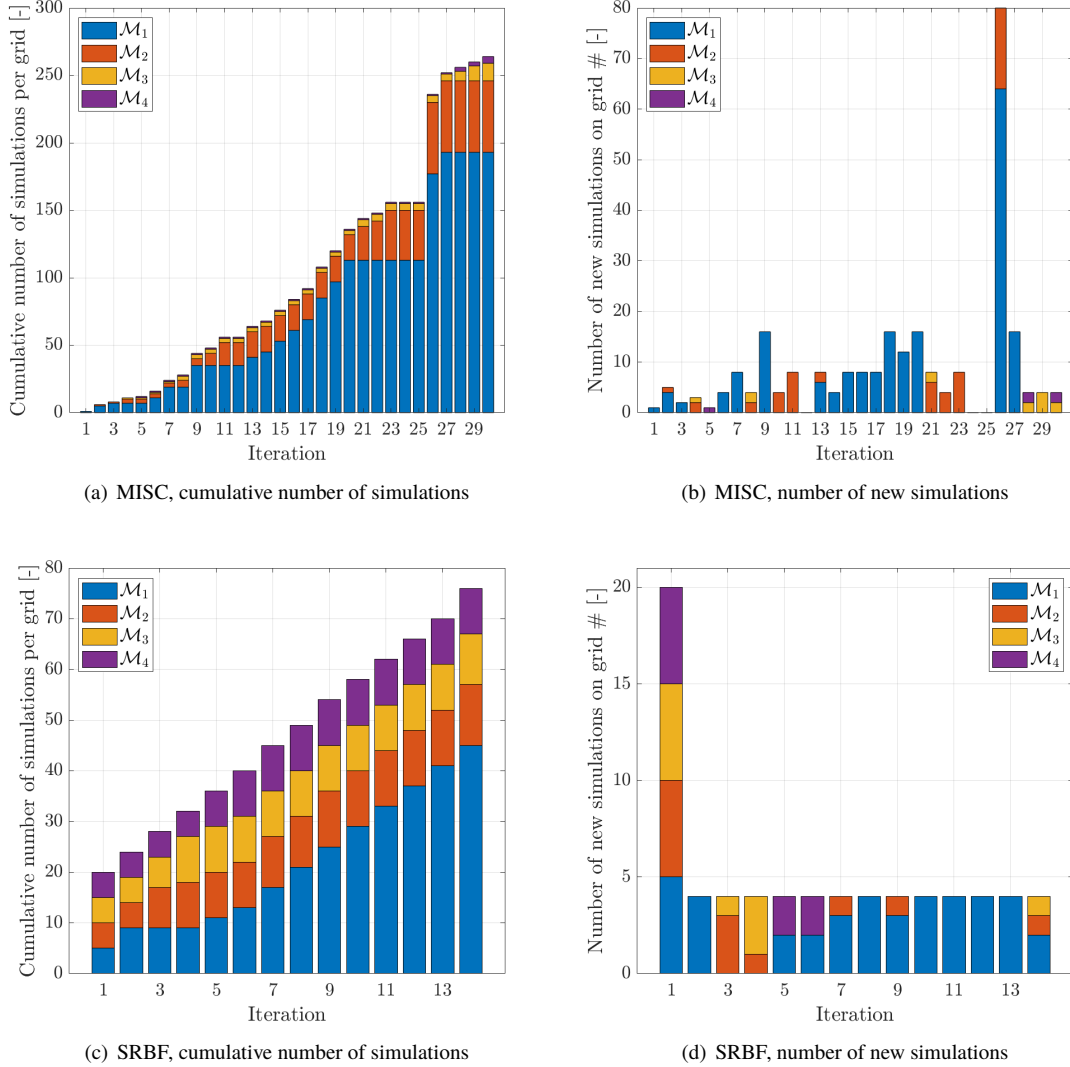


**Fig. 14 Comparison of MISC and SRBF results: number of simulations required at each iteration for each grid.**

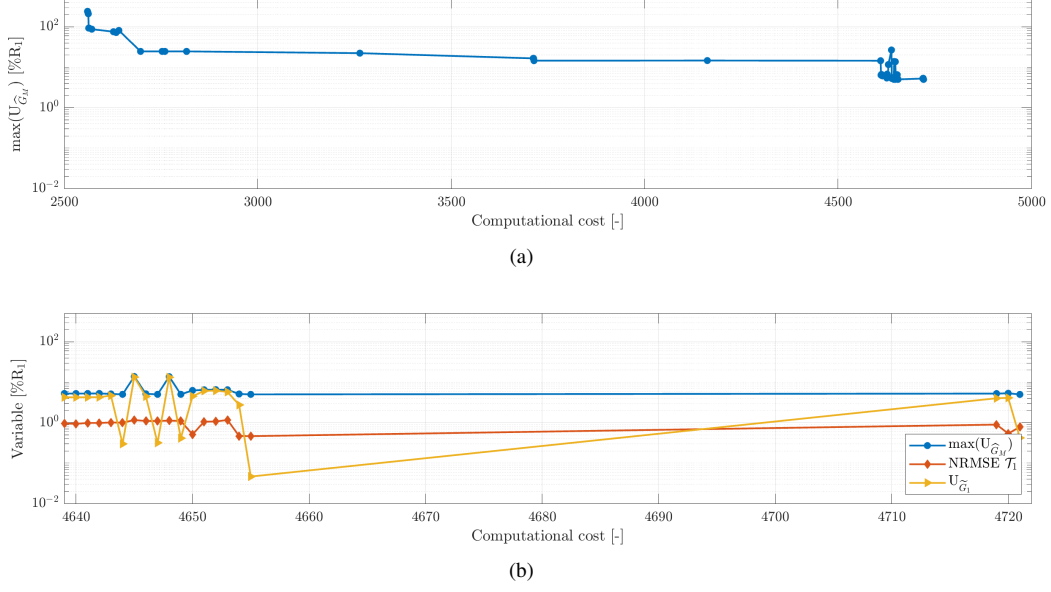


**Fig. 15** SRBF results: (a) convergence of the maximum prediction uncertainty and (b) its comparison with the lowest-fidelity prediction uncertainty and the normalized (with the function range) RMSE of  $\mathcal{T}_1$  versus the computational cost from iteration 8 to final.

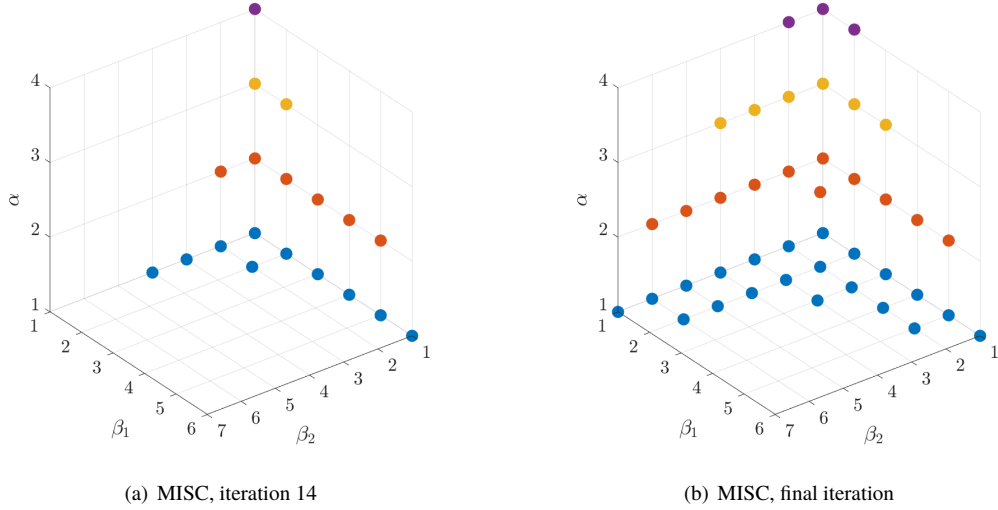


**Fig. 16** MISC results: explored multi-indices. The indices  $\beta_1$  and  $\beta_2$  determine how many quadrature points are selected according to the level function (2) for the advancement speed and the draught, respectively.

## V. Conclusions and Future Work

MISC and SRBF have been applied and compared for the UQ of a RoPax ferry advancing in calm water and subject to two operational uncertainties, namely the ship speed and draught (linked to the payload). The estimation of expected value, standard deviation, and probability density function of the (model-scale) resistance obtained by RANS computations has been discussed. Both MISC and SRBF used as multi-fidelity levels the multi-grid computations provided by the RANS solver. More specifically, four grids (obtained as isotropic coarsening of an initial grid) were available, and have been used. This implies that the multi-indices considered in MISC have just one component controlling the spatial discretization (instead of three), so that in total the dimension of the multi-indices is three (one

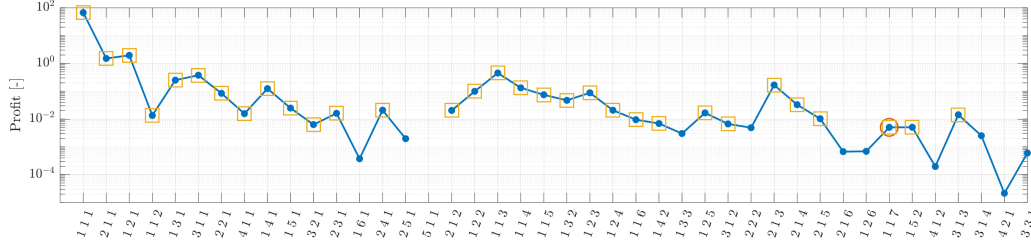


**Fig. 17 MISC results: profit of the explored multi-indices at the final iteration. The multi-indices circled in yellow have profit higher than the one marked in red and have been added to the index set  $I$  (see Algorithm 1).**

component for the spatial discretization plus two components for the parametric discretization).

Overall, MISC proved to be quite effective in delivering a reasonable approximation of the statistical indicators (expected value, standard deviation, probability density function) of the quantity of interest with a limited computational cost, but on the other hand turned out to be very sensitive to the numerical noise that affects the RANS solver, especially with the coarsest grid; this becomes clearly visible when the computational budget gets larger, as more runs of the RANS solver are considered. Strategies to mitigate this effect by smoothing the data coming from the RANS solver (e.g. by least-squares regression) are under investigation. Such smoothing could also take into account the soft information (monotonicity, multimodality, etc.) available on the physical nature of the problem. In this particular case, the resistance is expected to be monotone increasing with respect to advancement speed and draught: such property could be preserved by employing, e.g., least-squares regressions with appropriate polynomial degrees and/or monotonic smoothing, see e.g. [43]. Another practical problem is caused by the non-monotonic behavior of the profits, where some indices with low-profits shade useful neighbors, thus delay the convergence of MISC. More robust strategies to explore the set of multi-indices, that blend the profit-based selection of indices with other criteria are also subject of current work; see e.g. [30, 33], where this problem was discussed in the context of adaptive sparse-grids quadrature/interpolation.

The SRBF training also used mainly lowest-fidelity (and therefore lowest computational cost) RANS computations, as desired. Nevertheless, the initial training (first iteration) had a quite high computational cost, due to the use of RANS computations from all fidelity levels. Within the current computational effort, the convergence of expected value, standard deviation, and probability density function of the ship resistance is reasonably smooth, with quite small variations versus along the iteration. Moreover, the adaptive use of regressive SRBF has a beneficial effect on the robustness of the method to noisy data. Ongoing and future work focuses on the definition of a more efficient scheme for the initial training, as well as a data-adaptive criterion for the activation of the regressive model. Comparison with other methods, such as multi-fidelity Gaussian processes, will be also investigated.

MISC and SRBF give close values of expected value and standard deviation. The probability density functions are reasonably close, although the MISC surrogate model is affected by the noise in the data and its effects are visible in the resulting density function. Overall, the results suggest that MISC could be preferred when only a limited number of RANS computations is available. For larger data sets both MISC and SRBF represent a valid option, with a slight preference in favor of the current implementation of SRBF, due to its robustness to noise. Future research will address more complex test cases (larger number of uncertain parameters and more realistic conditions, such as regular/irregular waves) possibly validating the results against benchmark values.

## Acknowledgments

CNR-INM is grateful to Dr. Woei-Min Lin, Dr. Elena McCarthy, and Dr. Salahuddin Ahmed of the Office of Naval Research and Office of Naval Research Global, for their support through NICOP grant N62909-18-1-2033. Dr. Riccardo Pellegrini is partially supported through CNR-INM project OPTIMAE. The HOLISHIP project (HOListic optimisation of SHIP design and operation for life cycle, [www.holiship.eu](http://www.holiship.eu)) is also acknowledged, funded by the European Union's Horizon 2020 research and innovation program under grant agreement N. 689074. Lorenzo Tamellini and Chiara Piazzola have been supported by the PRIN 2017 project 201752HKH8 "Numerical Analysis for Full and Reduced Order Methods for the efficient and accurate solution of complex systems governed by Partial Differential Equations (NA-FROM-PDEs)". Lorenzo Tamellini also acknowledges the support of GNCS-INdAM (Gruppo Nazionale Calcolo Scientifico - Istituto Nazionale di Alta Matematica).

## References

- [1] He, W., Diez, M., Zou, Z., Campana, E. F., and Stern, F., “URANS study of Delft catamaran total/added resistance, motions and slamming loads in head sea including irregular wave and uncertainty quantification for variable regular wave and geometry,” *Ocean Engineering*, Vol. 74, 2013, pp. 189–217.
- [2] Diez, M., Broglia, R., Durante, D., Olivieri, A., Campana, E. F., and Stern, F., “Statistical Assessment and Validation of Experimental and Computational Ship Response in Irregular Waves,” *Journal of Verification, Validation and Uncertainty Quantification*, Vol. 3, No. 2, 2018.
- [3] Durante, D., Broglia, R., Diez, M., Olivieri, A., Campana, E., and Stern, F., “Accurate experimental benchmark study of a catamaran in regular and irregular head waves including uncertainty quantification,” *Ocean Engineering*, Vol. 195, 2020, p. 106685.
- [4] Diez, M., Campana, E. F., and Stern, F., “Stochastic optimization methods for ship resistance and operational efficiency via CFD,” *Structural and Multidisciplinary Optimization*, Vol. 57, No. 2, 2018, pp. 735–758.
- [5] Serani, A., Diez, M., Wackers, J., Visonneau, M., and Stern, F., “Stochastic shape optimization via design-space augmented dimensionality reduction and rans computations,” *57th AIAA Aerospace Sciences Meeting, SciTech 2019*, 2019, p. 2218.
- [6] Quagliarella, D., Serani, A., Diez, M., Pisaroni, M., Leyland, P., Montagliani, L., Iemma, U., Gaul, N. J., Shin, J., Wunsch, D., Hirsch, C., Choi, K., and Stern, F., “Benchmarking Uncertainty Quantification Methods Using the NACA 2412 Airfoil with Geometrical and Operational Uncertainties,” *57th AIAA Aerospace Sciences Meeting, SciTech 2019*, 2019, p. 3555.
- [7] Beran, P. S., Bryson, D. E., Thelen, A. S., Diez, M., and Serani, A., “Comparison of Multi-Fidelity Approaches for Military Vehicle Design,” *21th AIAA/ISSMO Multidisciplinary Analysis and Optimization Conference (MA&O), AVIATION 2020*, Virtual Event, June 15-19, 2020.
- [8] Giles, M. B., “Multilevel Monte Carlo Path Simulation,” *Operations Research*, Vol. 56, No. 3, 2008, pp. 607–617.
- [9] Cliffe, K., Giles, M., Scheichl, R., and Teckentrup, A., “Multilevel Monte Carlo methods and applications to elliptic PDEs with random coefficients,” *Computing and Visualization in Science*, Vol. 14, No. 1, 2011, pp. 3–15.
- [10] Haji-Ali, A.-L., Nobile, F., and Tempone, R., “Multi-index Monte Carlo: when sparsity meets sampling,” *Numerische Mathematik*, 2015, pp. 1–40.
- [11] Kuo, F. Y., Schwab, C., and Sloan, I., “Multi-level Quasi-Monte Carlo Finite Element Methods for a Class of Elliptic PDEs with Random Coefficients,” *Foundations of Computational Mathematics*, Vol. 15, No. 2, 2015, pp. 411–449.
- [12] Teckentrup, A. L., Jantsch, P., Webster, C. G., and Gunzburger, M., “A Multilevel Stochastic Collocation Method for Partial Differential Equations with Random Input Data,” *SIAM/ASA Journal on Uncertainty Quantification*, Vol. 3, No. 1, 2015, pp. 1046–1074.
- [13] Beck, J., Tamellini, L., and Tempone, R., “IGA-based Multi-Index Stochastic Collocation for random PDEs on arbitrary domains,” *Computer Methods in Applied Mechanics and Engineering*, Vol. 351, 2019, pp. 330 – 350.
- [14] Jakeman, J. D., Eldred, M., Geraci, G., and Gorodetsky, A., “Adaptive Multi-index Collocation for Uncertainty Quantification and Sensitivity Analysis,” *International Journal for Numerical Methods in Engineering*, Vol. 121, No. 6, 2020, pp. 1314–1343.
- [15] Haji-Ali, Abdul-Lateef, Nobile, Fabio, Tempone, Raúl, and Wolfers, Sören, “Multilevel weighted least squares polynomial approximation,” *ESAIM: M2AN*, Vol. 54, No. 2, 2020, pp. 649–677.
- [16] Peherstorfer, B., Willcox, K., and Gunzburger, M., “Survey of Multifidelity Methods in Uncertainty Propagation, Inference, and Optimization,” *SIAM Review*, Vol. 60, No. 3, 2018, pp. 550–591.
- [17] Gorodetsky, A., Geraci, G., Eldred, M. S., and Jakeman, J., “A generalized approximate control variate framework for multifidelity uncertainty quantification,” *Journal of Computational Physics*, Vol. 408, 2020, p. 109257.
- [18] Pisaroni, M., Nobile, F., and Leyland, P., “A Multilevel Monte Carlo Evolutionary Algorithm for Robust Aerodynamic Shape Design,” *18th AIAA/ISSMO Multidisciplinary Analysis and Optimization Conference. Denver, Colorado*, 2017.
- [19] Pisaroni, M., Nobile, F., and Leyland, P., “A Continuation Multi Level Monte Carlo (C-MLMC) method for uncertainty quantification in compressible inviscid aerodynamics,” *Computer Methods in Applied Mechanics and Engineering*, Vol. 326, 2017, pp. 20 – 50.

- [20] Geraci, G., Eldred, M. S., Gorodetsky, A., and Jakeman, J., “Recent advancements in Multilevel-Multifidelity techniques for forward UQ in the DARPA Sequoia project,” *57th AIAA Aerospace Sciences Meeting, SciTech 2019*, 2019, p. 0722.
- [21] Han, Z.-H., and Görtz, S., “Hierarchical kriging model for variable-fidelity surrogate modeling,” *AIAA journal*, Vol. 50, No. 9, 2012, pp. 1885–1896.
- [22] Baar, J. d., Roberts, S., Dwight, R., and Mallol, B., “Uncertainty quantification for a sailing yacht hull, using multi-fidelity kriging,” *Computers & Fluids*, Vol. 123, 2015, pp. 185 – 201.
- [23] Wackers, J., Visonneau, M., Pellegrini, R., Ficini, S., Serani, A., and Diez, M., “Adaptive N-Fidelity Metamodels for Noisy CFD Data,” *21th AIAA/ISSMO Multidisciplinary Analysis and Optimization Conference (MA&O), AVIATION 2020*, Virtual Event, June 15-19, 2020.
- [24] Serani, A., Pellegrini, R., Wackers, J., Jeanson, C.-J., Queutey, P., Visonneau, M., and Diez, M., “Adaptive multi-fidelity sampling for CFD-based optimization via radial basis functions metamodel,” *International Journal of Computational Fluid Dynamics*, Vol. 33, No. 6-7, 2019, pp. 237–255.
- [25] Han, Z.-H., Görtz, S., and Zimmermann, R., “Improving variable-fidelity surrogate modeling via gradient-enhanced kriging and a generalized hybrid bridge function,” *Aerospace Science and Technology*, Vol. 25, No. 1, 2013, pp. 177 – 189.
- [26] Di Mascio, A., Broglia, R., and Muscari, R., “On the application of the single-phase level set method to naval hydrodynamic flows,” *Computers & fluids*, Vol. 36, No. 5, 2007, pp. 868–886.
- [27] Di Mascio, A., Broglia, R., and Muscari, R., “Prediction of hydrodynamic coefficients of ship hulls by high-order Godunov-type methods,” *Journal of Marine Science and Technology*, Vol. 14, No. 1, 2009, pp. 19–29.
- [28] Broglia, R., and Durante, D., “Accurate prediction of complex free surface flow around a high speed craft using a single-phase level set method,” *Computational Mechanics*, Vol. 62, No. 3, 2018, pp. 421–437.
- [29] Trefethen, L. N., “Is Gauss quadrature better than Clenshaw-Curtis?” *SIAM Rev.*, Vol. 50, No. 1, 2008, pp. 67–87.
- [30] Gerstner, T., and Griebel, M., “Dimension-adaptive tensor-product quadrature,” *Computing*, Vol. 71, No. 1, 2003, pp. 65–87. <https://doi.org/10.1007/s00607-003-0015-5>, URL <http://dx.doi.org/10.1007/s00607-003-0015-5>.
- [31] Nobile, F., Tamellini, L., Tesei, F., and Tempone, R., “An adaptive sparse grid algorithm for elliptic PDEs with lognormal diffusion coefficient,” *Sparse Grids and Applications – Stuttgart 2014*, Lecture Notes in Computational Science and Engineering, Vol. 109, edited by J. Garcke and D. Pflüger, Springer International Publishing Switzerland, 2016, pp. 191–220.
- [32] Klimke, A., “Uncertainty modeling using fuzzy arithmetic and sparse grids,” Ph.D. thesis, Universität Stuttgart, Shaker Verlag, Aachen, 2006.
- [33] Chkifa, A., Cohen, A., and Schwab, C., “High-Dimensional Adaptive Sparse Polynomial Interpolation and Applications to Parametric PDEs,” *Foundations of Computational Mathematics*, Vol. 14, No. 4, 2014, pp. 601–633. <https://doi.org/10.1007/s10208-013-9154-z>.
- [34] Guignard, D., and Nobile, F., “A Posteriori Error Estimation for the Stochastic Collocation Finite Element Method,” *SIAM Journal on Numerical Analysis*, Vol. 56, No. 5, 2018, pp. 3121–3143.
- [35] Gutmann, H. M., “A radial basis function method for global optimization,” *Journal of global optimization*, Vol. 19, No. 3, 2001, pp. 201–227.
- [36] Forrester, A. I. J., and Keane, A. J., “Recent advances in surrogate-based optimization,” *Progress in aerospace sciences*, Vol. 45, No. 1-3, 2009, pp. 50–79.
- [37] Volpi, S., Diez, M., Gaul, N. J., Song, H., Iemma, U., Choi, K. K., Campana, E. F., and Stern, F., “Development and validation of a dynamic metamodel based on stochastic radial basis functions and uncertainty quantification,” *Structural and Multidisciplinary Optimization*, Vol. 51, No. 2, 2015, pp. 347–368.
- [38] Lloyd, S., “Least squares quantization in PCM,” *IEEE transactions on information theory*, Vol. 28, No. 2, 1982, pp. 129–137.
- [39] Li, X., Gao, W., Gu, L., Gong, C., Jing, Z., and Su, H., “A cooperative radial basis function method for variable-fidelity surrogate modeling,” *Structural and Multidisciplinary Optimization*, Vol. 56, No. 5, 2017, pp. 1077–1092.

- [40] Serani, A., Pellegrini, R., Broglia, R., Wackers, J., Visonneau, M., and Diez, M., “An Adaptive N-Fidelity Metamodel for Design and Operational-Uncertainty Space Exploration of Complex Industrial Problems,” *Proceedings of the 8th International Conference on Computational Methods in Marine Engineering (Marine 2019)*, 2019, pp. 177–188.
- [41] Wackers, J., Visonneau, M., Serani, A., Pellegrini, R., Broglia, R., and Diez, M., “Multi-Fidelity Machine Learning from Adaptive- and Multi-Grid RANS Simulations,” *Proceedings of the 33rd Symposium on Naval Hydrodynamics, Osaka, Japan*, 2020.
- [42] Serani, A., Leotardi, C., Iemma, U., Campana, E. F., Fasano, G., and Diez, M., “Parameter selection in synchronous and asynchronous deterministic particle swarm optimization for ship hydrodynamics problems,” *Applied Soft Computing*, Vol. 49, 2016, pp. 313 – 334.
- [43] Dykstra, R. L., and Robertson, T., “An Algorithm for Isotonic Regression for Two or More Independent Variables,” *The Annals of Statistics*, Vol. 10, No. 3, 1982, pp. 708–716.